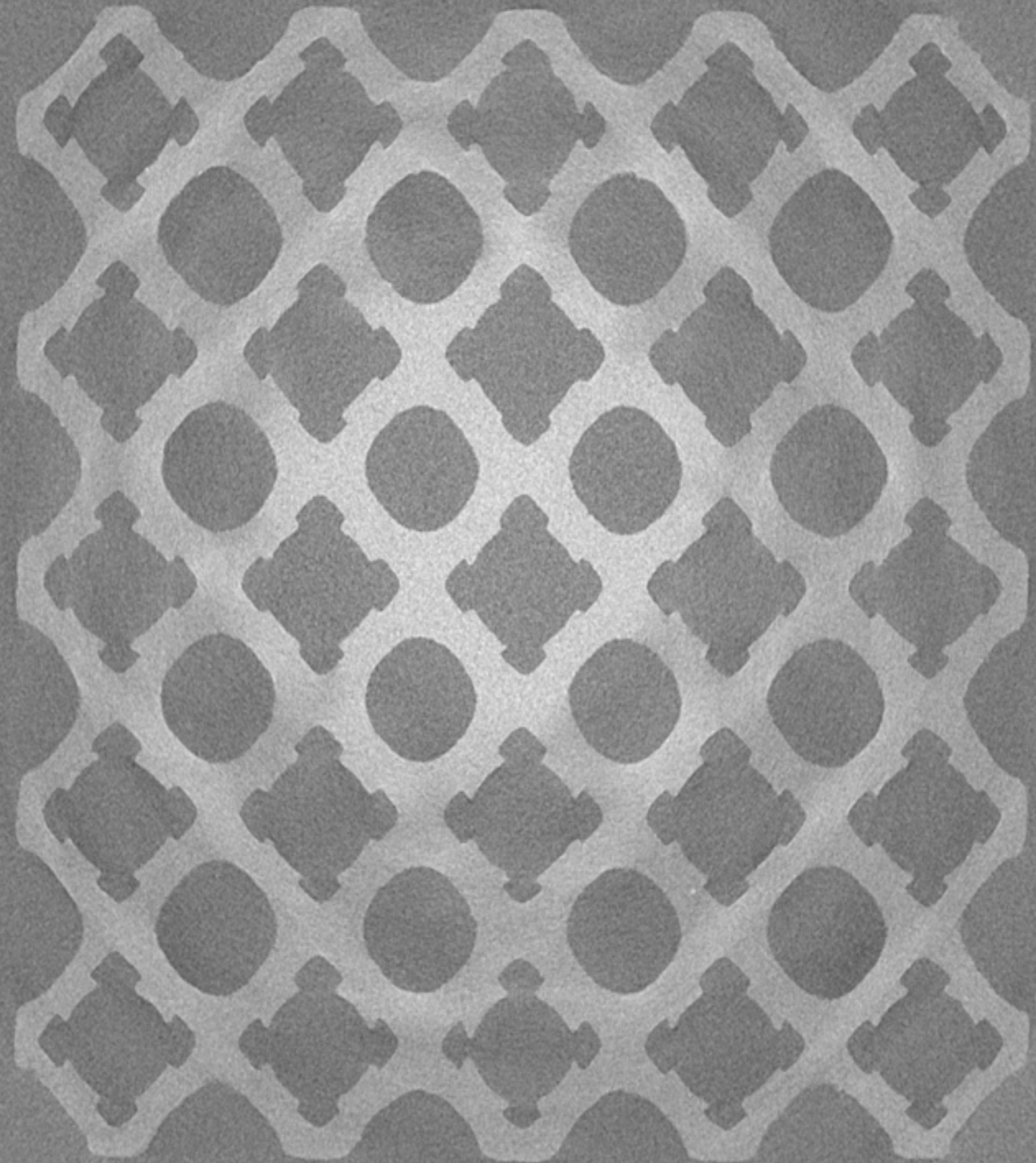


Meta-biomaterials with minimal surface morphology



Meta-biomaterials with minimal surface morphology

by

Alina Kuliesh

to obtain the degree of Master of Science
at the Delft University of Technology,

Student number: 4729625
Project duration: January 15, 2019 – August 15, 2019
Supervisor: Sebastien Callens, Prof. dr. Amir Zadpoor

An electronic version of this thesis is available at <http://repository.tudelft.nl/>.

Acknowledgements

During my master thesis project, I anticipated the moment when I would be writing the final part of the report — acknowledgements. But actually, it turned to be a sad moment, because a big part of my life, studying, finishes soon. So here I would like to acknowledge all the people without whom I could not have reach a high goal of becoming a Master of Science in Biomedical Engineering.

It is no exaggeration to assert that this project would be impossible without my daily supervisor Sebastien Callens. He eagerly responded to my email to give me research task for my master thesis, shared his great passion to TPMS structures and supported me through the whole project not only in the scientific sense but also emotionally. He helped me to get from the point when I did not know what TPMS is to performing experiments and simulations on the novel structures. I am honoured to have been working with my supervisor, Sebastien Callens, and wish him all the best in his scientific career.

Prof. dr. Amir Zadpoor has literally defined my fate already twice. When I was applying for this Master's programme, I was eager to follow Bioelectronics track and develop deep brain stimulation devices, but his speech at the freshmen master student gathering inspired me to follow the track he presented. His course Computational Biomechanics did not leave me a choice, in a good sense, which group to join for my final project. I have never regretted my decisions and further will try to stay in the orthopaedic biomaterials development field. I am extremely grateful to Prof. dr. Amir Zadpoor for an opportunity to conduct my research in his group.

To fabricate and measure the samples presented in this thesis I required help from other departments of our university. Tessa Essers and Joris van Dam from Digital Fabrication Lab printed all my samples, including many test prints. I always felt welcome in their lab and was surprised by their genuine interest in my project. The permeability measuring setup was provided by Karl Heller from Geoscience & Engineering Laboratory. Karl has spent a lot of hours with me in the lab searching for the best way to measure the samples, and our discussions were always a great distraction from the routine of the experiments.

I would also like to thank all the people who created and continue improving the Biomedical Engineering master program. This track perfectly suits people who have the mindset of an engineer, but their heart is with Medicine. The balanced combination of engineering and medical courses lectured by experts in their field won my heart forever. These two years were my greatest experience in higher education.

I am infinitely grateful to my mother Elena and father Igor. With the support of these two wonderful people, my brother and I have an opportunity to study in great places, follow our goals, develop our skills and most importantly feel loved and secured despite anything.

Another special man in my life is my grandfather Yakov, an exceptional engineer and the best storyteller. He will always remain for me the ideal person and an example to follow in life and career.

Last but definitely not least, I would like to express my gratitude to my husband Ivan, who was always by my side for the last four years and never let me give up or doubt myself. I thank him for going through every word of this report and giving valuable pieces of advice through the whole project.

Contents

Acknowledgements	iii
Abstract	vii
1 Introduction	1
1.1 Theory of TPMS	3
1.1.1 Minimal surface	3
1.1.2 Triply Periodic Minimal Surface	4
1.1.3 Porous solids	9
2 Methodology	11
2.1 Design	11
2.1.1 TPMS manipulations	11
2.1.2 Pore sizes	11
2.1.3 Regular and random designs	12
2.1.4 From the surface to the sheet solid	16
2.2 Fabrication	18
2.3 Porosity of the scaffolds	19
2.4 Permeability of the scaffolds	19
2.5 Mechanical testing of the scaffolds	21
2.6 Micro-CT scanning	22
2.7 COMSOL model	22
3 Results	25
3.1 Fabricated samples	25
3.2 Experimental results	26
3.2.1 Permeability test results	26
3.2.2 Mechanical test results	28
3.2.3 Relation between porosity and physical properties	31
3.2.4 Micro-CT scan results	37
4 Fluid dynamics simulation: tuning model and results	39
4.1 COMSOL model	39
4.1.1 Mesh	39
4.1.2 Physics	40
4.1.3 Boundary conditions	41
4.1.4 Study	41
4.2 Results	42
4.2.1 Velocities distribution	42
4.2.2 Wall shear stresses	44
4.2.3 Permeability values	46

5 Discussion	49
5.1 Experiment results	49
5.2 Fabrication issues	50
5.3 Quantitative model results.	50
5.4 Qualitative model results.	55
6 Conclusions and outlook	57
Appendices	59
A Combined experimental results	61
B Results of the t-test	63
C Failure modes of the samples	67
Bibliography	69

Abstract

Triply Periodic Minimal Surfaces (TPMS) have earned great popularity in porous meta-biomaterials by cause of unique mass transfer properties, tunable mechanical properties, large pore space and high surface to volume ratio. Numerical and experimental studies suggest a great potential for TPMS-based architectures in the treatment of segmental bone defects, where supporting scaffolds are crucial in bridging the gap unable to heal naturally. However, current studies are limited to investigating the properties of classic TPMS architectures. In this thesis, I present the design, fabrication and characterisation of a novel type of meta-biomaterials inspired by TPMS morphology. I show a practical application of Weierstrass equations to define Schwarz P, Schwarz D and Gyroid surfaces, which provides an opportunity to remove fundamental patches from the original surface and design unique structures. Moreover, one of the developed designs applied basics of graph theory to construct the material which mimics the randomness of the trabecular bone structure, while preserving the benefits of regular TPMS morphology. The results demonstrate the improved performance of the modified TPMS scaffolds compared to classic structures in terms of permeability and compliance properties, crucial for the materials applied in orthopaedic implants. The porosity and permeability values of the developed metamaterial were found to be in the range of trabecular bone. Additionally, the possibilities to simulate the mass transfer properties of the novel material were examined in COMSOL and valuable qualitative results, like fluid velocity distribution and flow-induced wall shear stress, retrieved. Overall my thesis introduces an innovative idea for biomaterial design and adds a strong argument in favour of TPMS morphology application in the orthopaedic material research field.



Introduction

The progress in material science and additive manufacturing is a driving force for developing new metamaterials with novel combinations of properties: mechanical, mass transfer, biological *etc.* Architected cellular solids with triply periodic minimal surface (TPMS hereinafter) morphology is an illustrative example of the advancement in this field. The deep mathematical background and periodicity of the structure contribute to the simplification of the design, reproducibility of samples and lowers computational cost of material behaviour simulations. Therefore TPMS architecture has been a focus of a growing amount of studies related to constructing materials, investigating their properties and discovering the interrelation between the morphology and material behaviour.

In the previous paragraph, I have already introduced the term TPMS. Main characteristics of the Triply Periodic Minimal Surface are encoded in the definition itself. The mathematical term minimal surface indicates a surface that locally minimises its area, triply periodic means that the surface is created by the translation of unit cell in three directions of an orthonormal basis in \mathbb{R}^3 . The first TPMS were introduced by Karl Schwarz, including Schwarz P ("Primitive") and Schwarz D ("Diamond") [49]. Later, Alan Schoen introduced Gyroid [48]. The minimal surfaces, mentioned above, are the most extensively studied and applied ones.

TPMS have earned great popularity in porous meta-biomaterials by cause of unique mass transfer properties, variable mechanical characteristics, large pore space and high surface to volume ratio. Moreover, similarities in morphological, mechanical and permeability properties between trabecular bone structure and TPMS scaffolds were recently reported [7, 9, 10, 22, 29, 37, 42, 56, 57].

Unique combination of high mechanical strength, relatively low Young's modulus and high yield stress were observed for TPMS scaffolds. However, in the study of Bobbert *et al.* the stiffness of the TPMS scaffolds, produced from biocompatible Ti alloy, significantly exceeded the range for trabecular bone [10], while permeability and porosity were consistent with it. That is why the implants, employing these structures, are prone to stress shielding and consequently bone degradation according to Wolff's law.

Good mechanical support at the early stages of bone healing and sufficient permeability of scaffolds are necessary conditions for regeneration processes [10, 58]. It was also discovered that surface curvature [7, 8, 45], pore shape and size [32, 34, 54], interconnectivity [32] can orchestrate bone tissue regeneration. For instance, pore sizes $>300 \mu m$ are advised due to enhanced osteogenesis and vascular growth into scaffold [32]. Small pores induce osteochondral ossification before osteogenesis [46]. Mechanical stimulation and fluid shear stress, in particular, are also considered to be important regulators of bone metabolism. It has been reported that fluid shear stress, generated by interstitial fluid flow, triggers bone cells to release osteogenic signalling factors [55].

The research goal of this thesis is to design, fabricate and investigate the mechanical and mass transfer properties of the scaffolds based on TPMS morphology with minor alterations introduced by means of fundamental patches excision. The changes in the classic geometry of TPMS are aimed to improve permeability and show the possibility of increasing the compliance of the structure. The developed approach allows these two essential characteristics of the material to reach values, desirable for orthopaedic implants.

Thesis outline

In the following section, I introduce theoretical concepts behind TPMS. Following that, in chapter 2, the established design process, fabrication, experiments applied to the scaffolds and the developed COMSOL model are described. Then in chapter 3, I cover the results of the experiment and Finite Element simulation. The thesis is finalised with a Discussion and Conclusion chapters 4,5.

1.1. Theory of TPMS

In this part of the report, the theoretical knowledge required for a better understanding of the thesis is provided. It includes basic theory of Triply Periodic Minimal Surfaces.

1.1.1. Minimal surface

As already mentioned, a minimal surface is a surface that locally minimises its area. A simple example of a minimal surface is a soap film spread over a randomly shaped frame without intersections.



Figure 1.1: Soap solution spread over the frame.

Like any physical system, soap film tends to minimise its energy according to the second law of thermodynamics. Surface energy, E , is proportional to the surface area, S , and can be described by formula $E = \sigma S$, where σ is a constant parameter, surface tension. Thus minimal energy corresponds to a minimal surface. Noteworthy, researchers in the field of TPMS also conducted soap film experiments in their work, which led to the discovery of different forms of TPMS.

The defining characteristics of minimal surfaces is zero value of mean curvature, H , and non-positive value of the Gaussian curvature, K , at every point on the surface [26, 48]. According to the equations 1.1, 1.2 the second regularity already follows from the first one.

$$H = \frac{\kappa_1 + \kappa_2}{2}, \quad (1.1)$$

$$K = \kappa_1 * \kappa_2, \quad (1.2)$$

where κ_1 and κ_2 are defined as principal curvatures of the surface at a given point as visualised in figure 1.2. In line with the definition $\kappa_1 = -\kappa_2$ in every point, minimal surfaces are as concave as they are convex, which is equivalent to the saddle- or flat-shaped surrounding of each point.

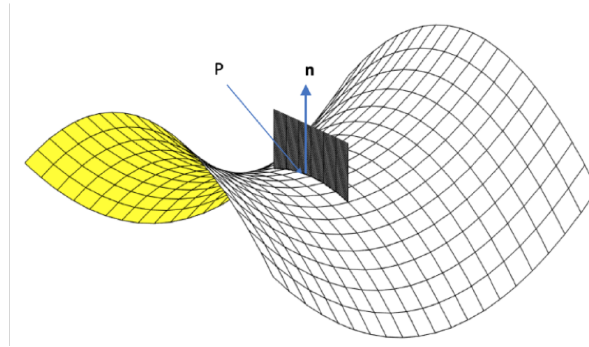


Figure 1.2: The normal plane, containing the normal vector, \mathbf{n} , to the surface at the point P, intersects with the surface and creates a planar curve. The curvature, κ_n , of this planar curve can be evaluated as a reciprocal of the radius of the osculating circle. If we let the normal plane rotate around the normal vector and calculate curvature at the same point P for each curve of intersection, the maximum, κ_1 , and minimum, κ_2 , values of κ_n are defined as principal curvatures.

1.1.2. Triply Periodic Minimal Surface

Structure: similar to a crystal structure, all TPMS consist of the simplest repeating unit called a unit cell or a lattice fundamental domain. Consequently, the properties of TPMS are defined on the level of unit cells. In figure 1.3 Schwarz P, Schwarz D and Gyroid unit cells are illustrated. However, even smaller building blocks can be identified in TPMS. These units under repeated symmetry operations, enable the construction of the infinite periodic surfaces. The smallest possible building blocks are fundamental patches. A unit cell can be constructed by proper attachment of patches to open edges of each other. The principles of the assembling were discovered by Schwarz and successfully applied later by other researchers. The principles comprised two rules: 1) if one of the boundaries of the fundamental patch is a straight line, the minimal surface can be smoothly continued across this line by 180° rotation; 2) if the fundamental patch meets the plane perpendicularly, the mirror reflection of the patch would smoothly continue the surface [17]. In figure 1.3 the unit cells of the TPMS, exploited in this thesis, are illustrated with the corresponding fundamental patches.

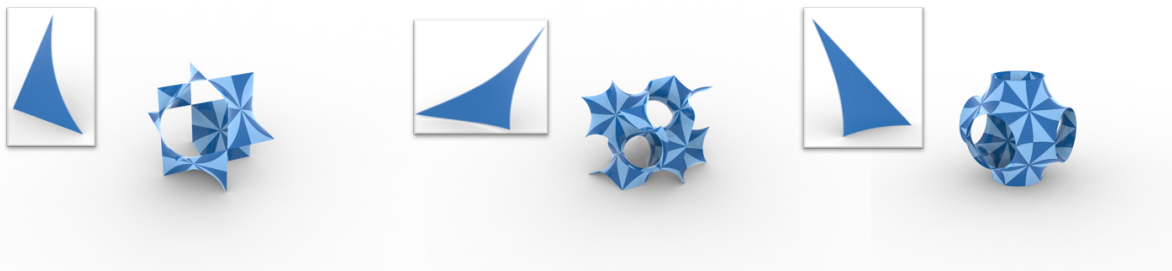


Figure 1.3: The unit cells of Schwarz D, Gyroid and Schwarz P with the fundamental patches highlighted in alternating colours. Shape of the single fundamental patch is presented next to each unit cell.

Parametrization: two great mathematicians of the nineteenth century Riemann and Weierstrass discovered equations which precisely define the minimal surface. These equations,

known as Weierstrass equations, consist of three integrals which parameterize the surface in terms of the complex analytic function $R(\omega)$ and map the complex plane to \mathbb{R}^3 . In Cartesian coordinates the equations take the following form [26]:

$$x = \operatorname{Re} \int_0^{\omega_0} e^{i\theta} (1 - \omega^2) R(\omega) d\omega, \quad (1.3)$$

$$y = -\operatorname{Im} \int_0^{\omega_0} e^{i\theta} (1 + \omega^2) R(\omega) d\omega, \quad (1.4)$$

$$z = \operatorname{Re} \int_0^{\omega_0} e^{i\theta} (2\omega) R(\omega) d\omega, \quad (1.5)$$

Integration is carried out on an arbitrary path from 0 to ω_0 in the integration domain on complex plane. In figure 1.4 the integration domains, indicated by shaded region, for G, P and D fundamental patches are illustrated. The function $R(\omega)$ determines the family of minimal surfaces, with the varying parameter — Bonnet angle, θ , named in honour of Ossian Bonnet. He was the first one to discover the isometric (preserving intrinsic properties) transformation between minimal surfaces [11]. For instance, Schwarz P, D and Gyroid belong to the same family, sharing the same function $R(\omega) = 1/\sqrt{1 - 14\omega^4 + \omega^8}$. Thus their fundamental patches can be transformed one into each other via bending and rolling [18]. In simple terms, along the track of Bonnet transformation (stretching and shrinking forbidden) from D surface into P surface Gyroid emerges. This happens at particular Bonnet angle, derived by Schoen, $\Delta\theta_G \simeq 38^\circ$.

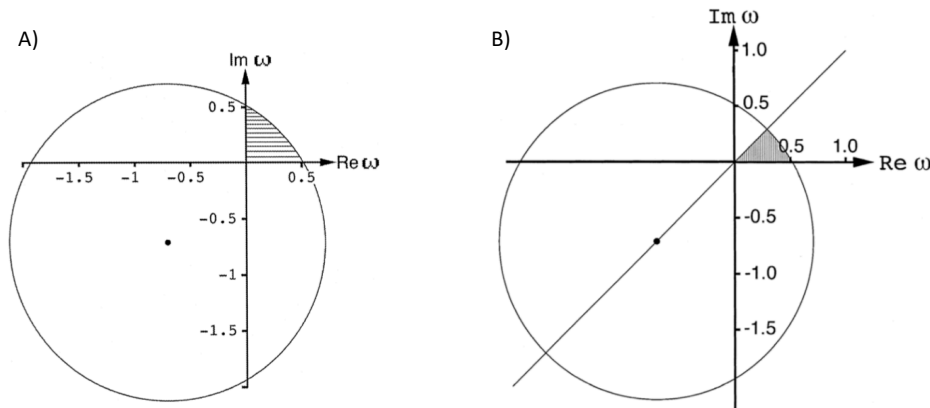


Figure 1.4: A) Integration domain for G fundamental patch [19]. B) Integration domain for P and D fundamental patches [20, 21]. The circular arc which limits the domain belongs to a circle of radius $\sqrt{2}$ centered at $(-\frac{\sqrt{2}}{2}, -\frac{\sqrt{2}}{2})$.

After performing the integration over the specified domain with substituted Bonnet angle for each surface (0° for D, 38° for G and 90° for P) the Cartesian coordinates X , Y , Z of each fundamental patch are defined. The scattered plots of fundamental patches are represented in figure 1.5. The density of points is defined by the amount of selected integration points in the integration domain.

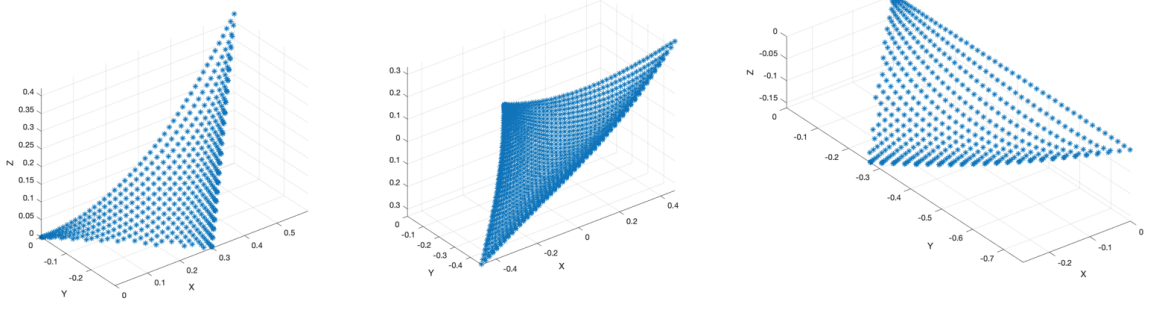


Figure 1.5: The scatter plots of D, G and P fundamental patches.

From fundamental patch to unit cell: to assemble the patches into a unit cell, two sequential steps should be implemented. First, twelve fundamental patches should be arranged into a skew hexagon, also called bounding cell. Then, multiple hexagons can be assembled into the unit cell. For P and G it takes eight skew hexagons, while D unit cell consists only of four hexagons.

The rules of merging fundamental patches were already described in the section 1.1.2. Here I only provide the tables 1.1, 1.2, 1.3 with the coordinate linear transformation of the single fundamental patch required to build one skew hexagon. The implementation was borrowed from the papers of Gandy *et al.*, but the major refinement was necessary to suit the requirements of my project [19–21].

Starting with the scatter plot of one fundamental patch, P1, and applying operations from the tables to each point of the scatter plot coordinates, constituting P1, the other fundamental patches, P2 — P12, are computed. This way, nodes of the surface, corresponding to the original fundamental patch, are created.

Table 1.1: Linear transformations of the D fundamental patch coordinates to evaluate the twelve fundamental patches which make up the skew hexagon of Schwarz D surface. Constants c_1 and c_2 equal $\frac{\sqrt{2}}{2}$ and $\frac{ap}{2}$ correspondingly.

Patch	X'	Y'	Z'
P ₁	$c_1(X - Y)$	$c_1(X + Y)$	Z
P ₂	$-c_1(X - Y) + c_2$	Z	$c_1(X + Y)$
P ₃	Z	$-c_1(X + Y) + c_2$	$c_1(X - Y)$
P ₄	$-c_1(X + Y) + c_2$	$-c_1(X - Y) + c_2$	$-Z + c_2$
P ₅	$-Z + c_2$	$c_1(X - Y)$	$-c_1(X + Y) + c_2$
P ₆	$c_1(X + Y)$	$-Z + c_2$	$-c_1(X - Y) + c_2$
P ₇	$-c_1(X - Y) + c_2$	$-c_1(X + Y) + c_2$	$-Z + c_2$
P ₈	$c_1(X - Y)$	$-Z + c_2$	$-c_1(X + Y) + c_2$
P ₉	$-Z + c_2$	$c_1(X + Y)$	$-c_1(X - Y) + c_2$
P ₁₀	$c_1(X + Y)$	$c_1(X - Y)$	Z
P ₁₁	Z	$-c_1(X - Y) + c_2$	$c_1(X + Y)$
P ₁₂	$-c_1(X + Y) + c_2$	Z	$c_1(X - Y)$

Table 1.2: Linear transformations of the G fundamental patch coordinates to evaluate the twelve fundamental patches which make up the skew hexagon of the Gyroid. Constants c_1 and c_2 equal $\frac{\sqrt{2}}{2}$ and $\frac{a_G}{8}$ correspondingly.

Patch	X'	Y'	Z'
P ₁	$-c_1(X + Y)$	$-c_1(X - Y) + 2c_2$	$Z + 3c_2$
P ₂	$c_1(X - Y)$	$-c_1(X + Y) + 2c_2$	$-Z + 3c_2$
P ₃	$-c_1(X - Y) + 2c_2$	$Z + 3c_2$	$c_1(X + Y) + 4c_2$
P ₄	$-c_1(X + Y) + 2c_2$	$-Z + 3c_2$	$c_1(-X + Y) + 4c_2$
P ₅	$Z + 3c_2$	$c_1(X + Y) + 4c_2$	$c_1(X - Y) + 2c_2$
P ₆	$-Z + 3c_2$	$c_1(-X + Y) + 4c_2$	$c_1(X + Y) + 2c_2$
P ₇	$c_1(X + Y) + 4c_2$	$c_1(X - Y) + 2c_2$	$-Z + c_2$
P ₈	$c_1(-X + Y) + 4c_2$	$c_1(X + Y) + 2c_2$	$Z + c_2$
P ₉	$c_1(X - Y) + 2c_2$	$-Z + c_2$	$-c_1(X + Y)$
P ₁₀	$c_1(X + Y) + 2c_2$	$Z + c_2$	$c_1(X - Y)$
P ₁₁	$-Z + c_2$	$-c_1(X + Y)$	$-c_1(X - Y) + 2c_2$
P ₁₂	$Z + c_2$	$c_1(X - Y)$	$-c_1(X + Y) + 2c_2$

Table 1.3: Linear transformations of the P fundamental patch coordinates to evaluate the twelve fundamental patches which make up the skew hexagon of Schwarz P surface. Constants c_1 and c_2 equal $\frac{\sqrt{2}}{2}$ and $\frac{a_P}{4}$ correspondingly.

Patch	X'	Y'	Z'
P ₁	$-c_1(X + Y)$	$Z + c_2$	$-c_1(X - Y) + 2c_2$
P ₂	$-c_1(X + Y)$	$-c_1(X - Y) + 2c_2$	$Z + c_2$
P ₃	$Z + c_2$	$-c_1(X + Y)$	$-c_1(X - Y) + 2c_2$
P ₄	$-c_1(X - Y) + 2c_2$	$Z + c_2$	$-c_1(X + Y)$
P ₅	$-c_1(X - Y) + 2c_2$	$-c_1(X + Y)$	$Z + c_2$
P ₆	$Z + c_2$	$-c_1(X - Y) + 2c_2$	$-c_1(X + Y)$
P ₇	$c_1(X - Y)$	$-Z + c_2$	$c_1(X + Y) + 2c_2$
P ₈	$c_1(X - Y)$	$c_1(X + Y) + 2c_2$	$-Z + c_2$
P ₉	$-Z + c_2$	$c_1(X - Y)$	$c_1(X + Y) + 2c_2$
P ₁₀	$c_1(X + Y) + 2c_2$	$-Z + c_2$	$c_1(X - Y)$
P ₁₁	$c_1(X + Y) + 2c_2$	$c_1(X - Y)$	$-Z + c_2$
P ₁₂	$-Z + c_2$	$c_1(X + Y) + 2c_2$	$c_1(X - Y)$

The parameter a is a unit cell size of the surface implicitly defined by Weierstrass equations and integration domain. For the selected integration domains presented in figure 1.4, $a_G = 2.6562, a_D = 1.6857, a_P = 2.1565$. The result of implementing the transformations is represented in figure 1.6. Each fundamental patch is highlighted in different colour.

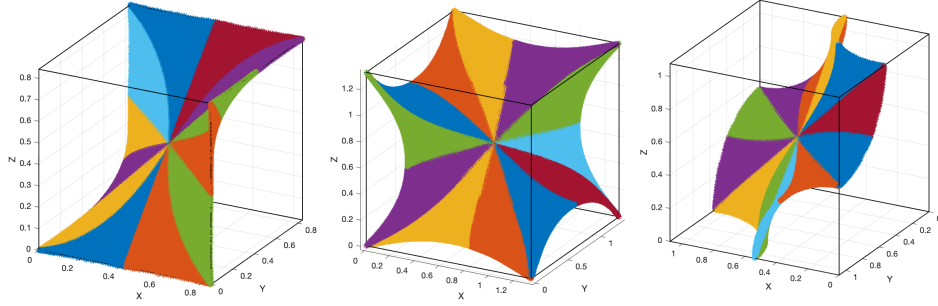


Figure 1.6: Scatter plots of D, G and P bounding cells (also referred to as skew hexagons).

The coordinates of the twelve patches all together comprise a so-called bounding cell, specific for each surface. These bounding cells undergo linear transformations according to the tables 1.4 — 1.6 and finally are assembled together into the unit cell.

Table 1.4: Linear transformations of the D bounding cell coordinates to evaluate the four skew hexagons which make up the unit cell of Schwarz D surface. Constant c_3 equals $\frac{a_D}{2}$.

Hexagon	X''	Y''	Z''
H ₁	$-Y' + c_3$	$-X' + c_3$	Z'
H ₂	Y'	$-X'$	$Z' - c_3$
H ₃	$Y' - c_3$	$X' - c_3$	Z'
H ₄	$-Y'$	X'	$Z' - c_3$

Table 1.5: Linear transformations of the G bounding cell coordinates to evaluate the eight skew hexagons which make up the unit cell of Gyroid. Constant c_3 equals $\frac{a_G}{2}$.

Hexagon	X''	Y''	Z''
H ₁	X'	Y'	Z'
H ₂	$-X' + 2c_3$	$-Y' + c_3$	Z'
H ₃	$-X' + c_3$	$Y' + c_3$	Z'
H ₄	$X' + c_3$	$-Y' + 2c_3$	Z'
H ₅	X'	$-Y' + c_3$	$Z' - c_3$
H ₆	$-X' + 2c_3$	Y'	$Z' - c_3$
H ₇	$-X' + c_3$	$-Y' + 2c_3$	$Z' - c_3$
H ₈	$X' + c_3$	$Y' + c_3$	$Z' - c_3$

Table 1.6: Linear transformations of the P bounding cell coordinates to evaluate the eight skew hexagons which make up the unit cell of Schwarz P surface.

Hexagon	X''	Y''	Z''
H ₁	X'	Y'	Z'
H ₂	$-X'$	Y'	Z'
H ₃	X'	$-Y'$	Z'
H ₄	$-X'$	$-Y'$	Z'
H ₅	X'	Y'	$-Z'$
H ₆	$-X'$	Y'	$-Z'$
H ₇	X'	$-Y'$	$-Z'$
H ₈	$-X'$	$-Y'$	$-Z'$

After the applied transformations to the bounding cells, the distribution of the points in three unit cells is computed. In figure 1.7 unit cells are illustrated with each skew hexagon highlighted with different colour.

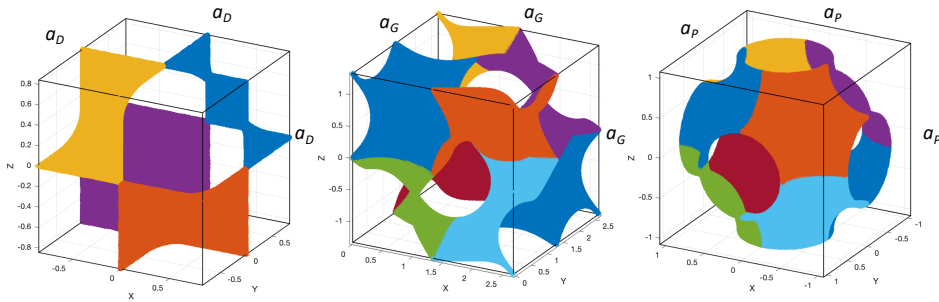


Figure 1.7: Scatter plots of D, G and P unit cells.

The infinite surface can be generated by appropriate translations of these domains. It involves shifts on the size of the unit cell in three orthogonal directions which coincide with the orthonormal basis of the unit cell.

This finalises the mathematical foundations of the conventional TPMS.

1.1.3. Porous solids

There are two major types of TPMS scaffolds design: sheet solids and network solids presented in figure 1.8 [30]. These approaches can be distinguished by the number of void domains (labyrinths) they possess. Minimal surface sheet solids follow the structure of an arbitrary TPMS, but walls of labyrinths have a non-zero thickness. Thus sheet solids have two non-intersecting void domains. The second architecture of scaffolds (network solids) is designed by complete filling one of the void domains with a material — one void domain remains. For my thesis, all the samples were designed as sheet solids because my final goal was to improve the permeability of the material, while filling one of the void domains clearly impairs this property.



Figure 1.8: On the left sheet solid architecture of 2x2x2 Gyroid unit cells. On the right network solid with the same structure.

The thickness given to the surface affects the mechanical and mass transfer properties of the scaffolds significantly. Samples with thicker walls can sustain higher mechanical loads, while the permeability properties follow the opposite trend [10]. Previously, the wall thickness and the unit cell size were the only variables in the design of TPMS sheet solids. In this thesis, a new approach to alter mechanical and permeability properties is developed. The idea is based on the fact that Schwarz P, Schwarz D and Gyroid TPMS are balanced TPMS and, according to the definition of balanced surface, they separate space into two disconnected congruent labyrinths. Thus any substance which entered one labyrinth can not advance to another. By the introduction of extra connections between the labyrinths, mass transfer and compliance of the scaffolds can be improved. These additional pores can be created by means of fundamental patches removal. In more detail, the design of the new type of metamaterials will be discussed in section 2.1.

2

Methodology

2.1. Design

In this section, I present the developed approach of TPMS geometry manipulation. This technique was aimed to create a new type of metamaterial with improved mass transfer and mechanical properties.

Material geometry was altered to answer the central question of this research: can mass transfer properties and compliance of the material be improved by introduction of extra channels, connecting two labyrinths. The developed designs of the novel metamaterial were aimed to strike a balance between permeability and stiffness for the future applications in bone tissue implants.

2.1.1. TPMS manipulations

Suppose that we have a surface composed of N_x by N_y by N_z unit cells. As we already know, the minimum unit of TPMS is a fundamental patch. One of the methods to achieve labyrinths interconnection is to remove fundamental patches from the surface in a regular or random way, with the restriction that the structure keeps its connectivity. When we move further and make a transition from a surface to a solid scaffold for tissue engineering purposes the restrictions on the number of removed units is imposed on the part of mechanical and biological properties of the scaffold. The requirements regarding the pore sizes from *in vitro* and *in vivo* studies suggest that pore sizes $\geq 300\mu m$ are recommended [32]. The target values for porosity and stiffness follow from the biomimetic approach to optimise the integration of the prosthesis. The range of Young's modulus for trabecular bone lies between $10MPa$ and $1570MPa$ [25]. The porosity equals 50%-90% [31]. A fairly high degree of variation follows from a great number of parameters influencing the trabecular bone structure: body part, age, sex, health conditions *etc.*

2.1.2. Pore sizes

To design structures, according to the novel idea of this thesis, the hole size originating from the fundamental patch excision should have been estimated. For our purposes, rough estimation of the critical pore diameter, the diameter of the largest sphere that can freely

pass through a pore, was applicable. The approach entails that the pore size can be approximated by the inscribed circle of the polygon maximally close to the pore shape. The diameter of the incircle equals to the ration of the polygon area to its perimeter:

$$d_{incircle} = \frac{S}{P}, \quad (2.1)$$

Previously considered fundamental patches of Schwarz P, Schwarz D and Gyroid surfaces have three vertices and can be represented by a triangular saddle-shaped patch as shown in figure 2.1. From the Heron's formula, it follows that the radius of an incircle in a triangle with sides of length A, B, C is given by:

$$r_{incircle} = \sqrt{\frac{(p-A)(p-B)(p-C)}{p}}, \quad (2.2)$$

where $p = \frac{P}{2}$. The lengths of the sides are computed as the distance between the vertices.

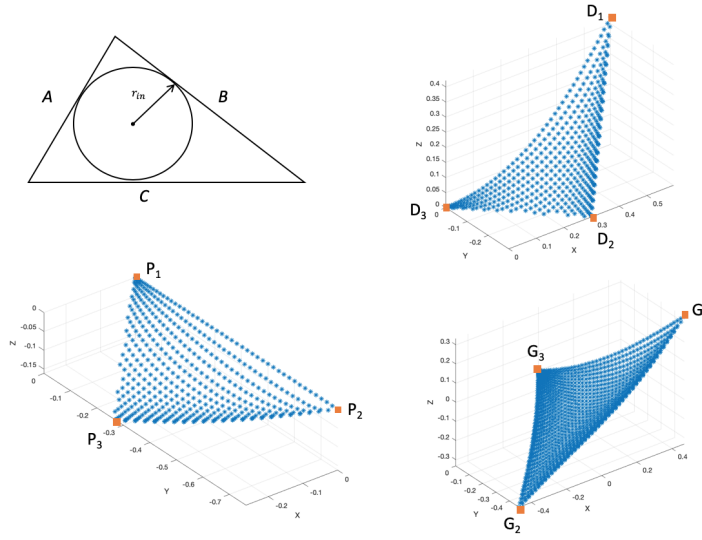


Figure 2.1: Approximation of D, G, P fundamental patches by a triangle $D_1D_2D_3$, $G_1G_2G_3$, $P_1P_2P_3$ correspondingly.

The diameters of the incircles for one fundamental patch, d_1 , and two adjacent fundamental patches, d_2 , for each surface type with the unit cell size of 2 mm are presented in the table 2.1:

Table 2.1: Incircle diameters. Pore size estimation.

	Schwarz D	Gyroid	Schwarz P
$d_1(\mu m)$	339	309	248
$d_2(\mu m)$	518	518	408

2.1.3. Regular and random designs

Taking into account the above requirements and estimated pore sizes, I developed five material designs built on Schwarz P geometry (four regular and one random); four — on

Schwarz D and Gyroid geometries (three regular and one random for each) with the unit cell size of 2 mm. The computational and fabrication complexity and the geometry standards of the specimens in the compression test were balanced by the previously specified size [27].

There is one major difference between regular and random approaches. In the regular design, the modifications (patches excision) are applied to a single unit cell, while in the random design, the starting point is the whole structure composed of multiple unit cells. This way the translation symmetry is preserved only in a regularly designed scaffolds. It will be explained in more detail further.

Schwarz P regular designs: in the figure 1.7 Schwarz P unit cell is illustrated. The regular redesign goal is to remove fundamental patches from the unit cell, preserving the structural connectivity when spanning the volume with unit cells. .

Even though there are a lot of different possibilities to remove fundamental patches, I have decided on the following four designs, presented in the figure below:

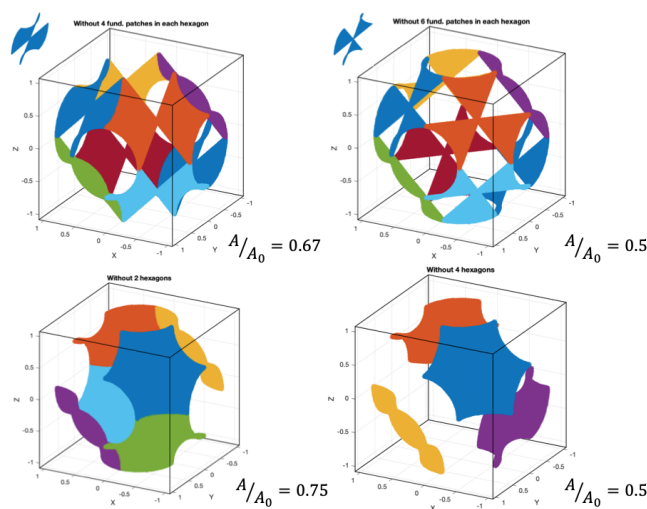


Figure 2.2: Four unit cells with alternative designs of the P unit cell. On top the designs with the changes introduced to the skew hexagon geometry. Below the unit cells without two (left) and four hexagons (right) in one unit cell. Next to each design the ratio between the area of the modified unit cell, A , and the original one, A_0 , is added.

Each of the modified cells meets the following criteria:

- the incircle diameter of the introduced holes in the surface is more than 300 μm ;
- the structure of connected unit cells does not lose its integrity.

However, for the design *without four skew hexagons* non-connected hexagons, located at the corners of the spanned volume (two at the top and two at the bottom), had to be removed. On top, it was orange and blue hexagons from the unit cells in opposite corners, at the bottom purple and yellow ones from another opposing pair of corners.

Schwarz D and Gyroid regular designs: the same criteria were applied to the alterations in Schwarz D and Gyroid unit cells geometries. Only four skew hexagons comprise one D unit cell, maximum one skew hexagon could be removed. In the figure 2.3 three designs originating from the D geometry are illustrated:

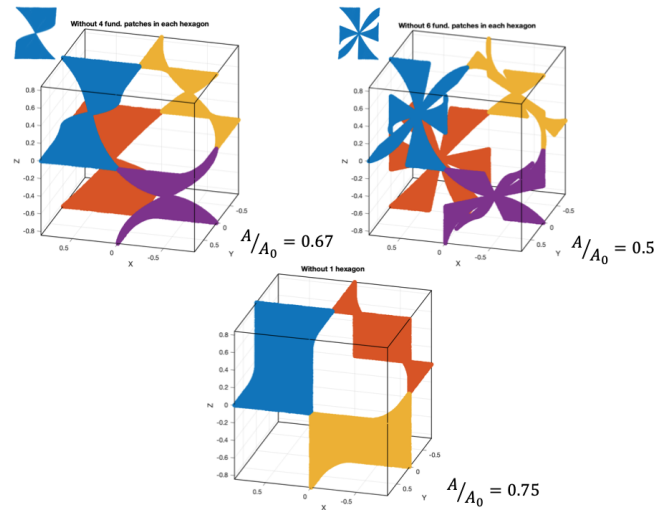


Figure 2.3: Three unit cells with alternative designs of the D unit cell. On top the designs with the changes introduced to the skew hexagon geometry. Below the unit cells with one hexagon removed.

The three designs for Gyroid morphology are presented further in figure 2.4. The skew hexagon without six fundamental patches, used for the D and P variations, did not contribute to the current geometry due to the small hole sizes.

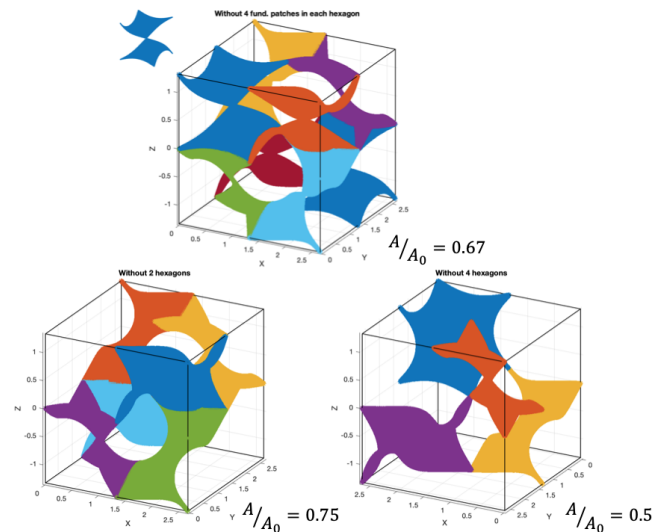


Figure 2.4: Three unit cells with alternative designs of the G unit cell. On top the Gyroid unit cell with skew hexagons without four fundamental patches. Below the unit cells without two (left) and four (right) hexagons.

Random designs: as I already mentioned for random designs the starting point is the whole structure of N_x by N_y by N_z unit cells. For my project the selected values were: $N_x = 5$, $N_y = 5$ and $N_z = 8$. This way the scaffolds can be inscribed in a cuboid with the dimensions $10\text{ mm} \times 10\text{ mm} \times 16\text{ mm}$. In the figure 2.5 three initial surfaces are presented.

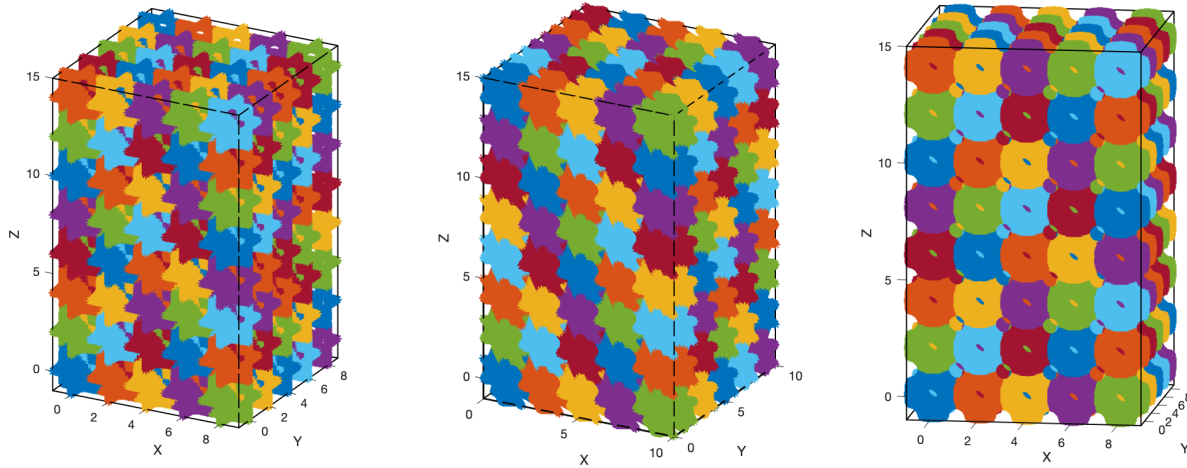


Figure 2.5: By this moment one should easily recognise the surfaces, which are from left to right are D, G, P surfaces. Each structure consists of $5 \times 5 \times 8$ unit cells each. Unit cell is differently coloured. The orientation of P structure is a different, making the labyrinths more visible.

In these structures, each fundamental patch has either two or three neighbouring fundamental patches. Two neighbours correspond to patches which constitute boundary layer, while internal fundamental patches have three neighbours. The patches are defined as neighbours if they share one side. Thus the whole structure can be converted to an undirected connected graph. In this graph, each node matches a fundamental patch, and the graph edges establish connections between the neighbour patches. Since one P or G unit cells already has $12 \times 8 = 96$ fundamental patches and D — $12 \times 4 = 48$, for clarity, I provide an example of graphs representing each unit cell:

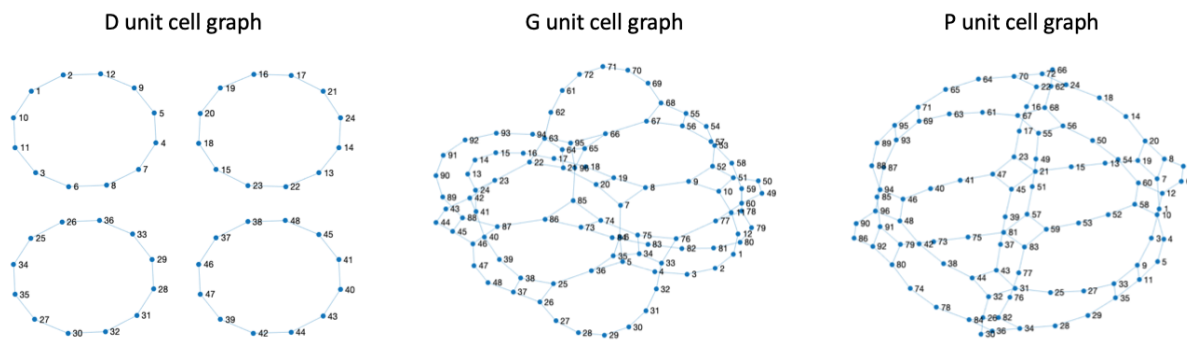


Figure 2.6: Connected graphs of the D, G and P unit cells. Each dot is a graph node representing fundamental patch in a unit cell, while edges connecting nodes represent shared patch boundaries.

Apparent difference of the D graph compared to the P and G is attributed to the fact that all the hexagons in the D unit cell do not share a common edge with each other. To go from

one unit cell graph to the graph of the whole structure, one extra step should be taken: all unit cells should be added and the connections between them established.

The idea of the random scaffold design is as follows:

- create a sequence of visiting nodes in the graph. It can be a list of nodes in ascending or descending order, as well as randomly generated. Depth-first search (DFS) algorithm with different root nodes can also be applied to generate the node sequence;
- going through the list, check whether it is possible to remove the node and at least one of its neighbours so that the graph remains connected, and hence the scaffold;
- if so delete the nodes from the graph and corresponding patches from the surface, else move on with the list.

The other minor requirements I imposed on the algorithm for the rationality of the design were: the boundary patches (ones which touch the bounding cuboid) are prohibited from removing, and all the remaining patches should have at least two neighbouring ones to prevent an excessive amount of pores. Again for simplicity, I illustrate the processed surfaces with only two unit cells arranged vertically, though the developed procedure is applicable for arbitrary dimensions (multiple of unit cell size) of the surface:

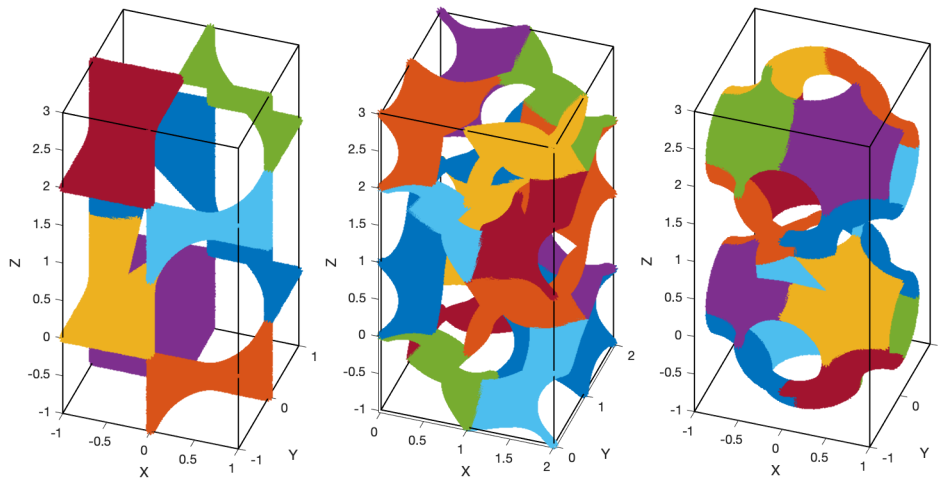


Figure 2.7: From left to right: D, G, P $1 \times 1 \times 2$ unit cell structures with randomly removed patches. The path through the graph was defined by the DFS algorithm.

2.1.4. From the surface to the sheet solid

All the previously described steps of the scaffold's design result in a scatter of points on the surface, so-called point cloud. With the help of an open-source software MeshLab a point cloud can be converted to a solid [12]. In MeshLab the triangular mesh is built on the given points interpolating the shape of the designed surface. Next, an offset mesh is created, contouring the original one and closing the gap between them. In more detail:

1. the file with *PLY* extension, containing the coordinates of the points, is imported into MeshLab;

2. the surface is reconstructed with the Ball Pivoting algorithm (three nodes form a face if the ball with specified radius R touches them without containing any other point) [6];
3. with the Marching Cube algorithm the surface is given thickness of $200 \mu m$, this way the aimed porosity of the samples is in the range of trabecular bone porosity;
4. the final structure is exported as an *STL* file for further processing.

An example in the figure 2.2 with Schwarz P surface design without two hexagons in each unit cell illustrates previously described steps:

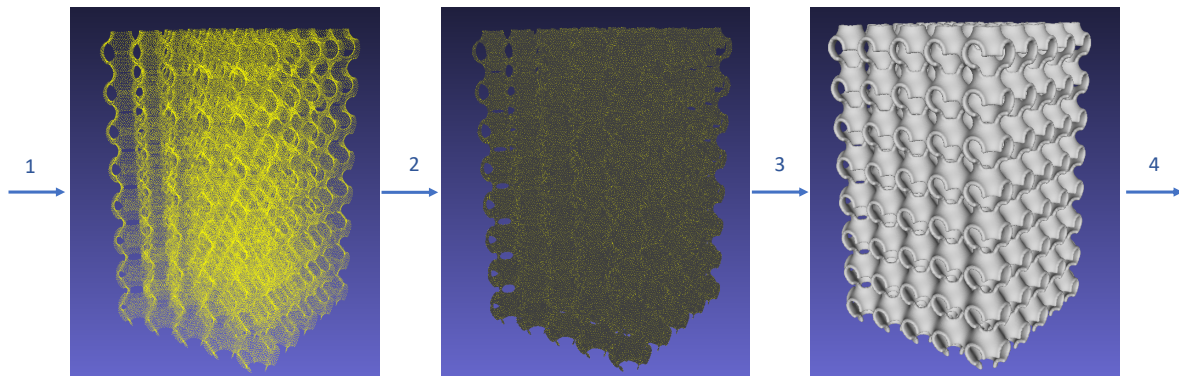


Figure 2.8: Applied sequence of steps to Schwarz P without 2 hexagons $5 \times 5 \times 8$ unit cells design. Numbers above the arrows correspond to the step number in the list.

An important point that in the MeshLab when the surface is converted into solid double surface is built on the inside and outside of the original one and the gap between is closed to create a continuous surface. This procedure has a side effect of filling the pores and reducing their initial size by approximately 40%, depending on the geometry. This effect is illustrated in the figure 2.9.

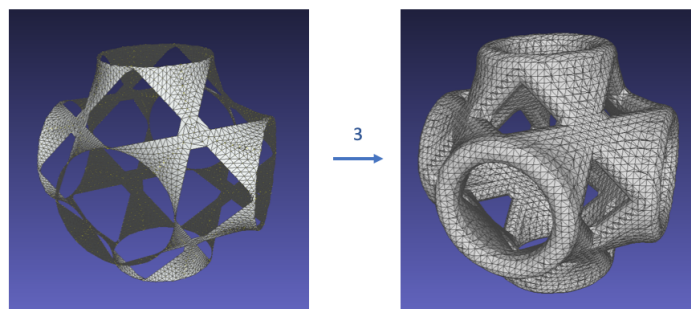


Figure 2.9: Conversion of Schwarz P unit cell surface (without 6 fundamental patches in each hexagon) into the solid.

2.2. Fabrication

Due to the complex morphology, TPMS scaffolds are mostly fabricated by means of additive manufacturing (3D printing). The material selection and dimensions of the structure define the suitable printing process. Two similar techniques: selective laser melting (SLM) and selective laser sintering (SLS) are commonly used to produce structures from metal alloys and thermoplastics on the microscale [10, 22, 51]. Another relatively fast and cheap method of printing on the submicron scale is stereolithography (SLA). The latter was the printing process applied to fabricate the samples for this research.

A resulting *STL* file can be used as an input file for Stereolithographic (SLA) 3D printer. The one I worked with to print my samples was FormLabs, Form2 SLA 3D printer. According to the SLA concept a laser is used to cure liquid resin into hardened plastic. The critical characteristics of the printer and the material used are summarised in the table 2.2. After printing the samples, IPA rinsing is required to remove excessive resin and post-curing — for improvement of mechanical properties.

Table 2.2: 3D printer and printing material properties [3, 4]

3D printer		Grey Pro material (post-cured)			
Laser Spot Size	Layer Thickness	Ultimate Tensile Strength	Tensile Modulus	Elongation	Flexural Modulus
140 μm	50 μm	61 MPa	2.6 GPa	13%	2.2 GPa

To minimise the risks of print failure, in the PreForm software the supports for the structure are generated [1]. They reinforce overhangs and other weak areas and should be removed after post-curing. Since the support pins are continuously connected to the samples at touchpoints, it is difficult to remove them without damaging the structure. To mitigate sample damage, I used support pins, originating from the raft, only at the bottom of my model as presented in the figure 2.10.

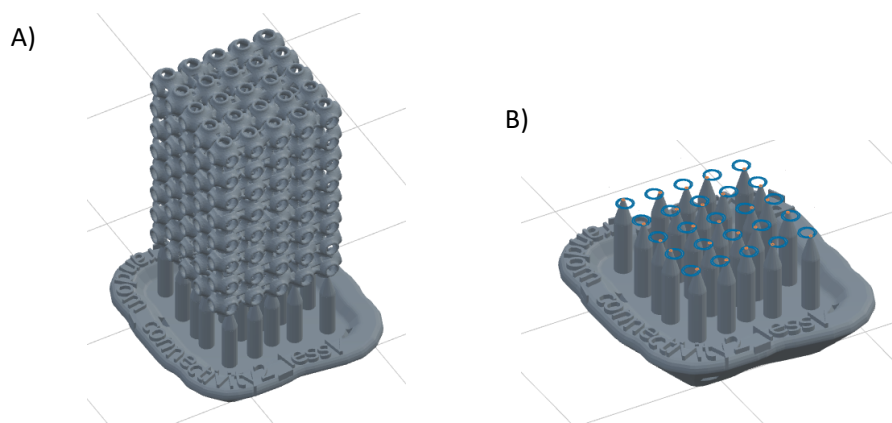


Figure 2.10: A) A visualisation of the *STL* file with P random surface design $5 \times 5 \times 8$ unit cells opened in the PreForm software with generated support scaffolds and raft. B) Print layer where the support meets the sample walls, touchpoint size equals 0.2 mm.

There are no strict instructions from the manufacturer how to remove the support without damaging the structure, but the laboratory tests showed that the support pins were easier to cut off after heating the sample at 70°C for 6-8 minutes.

2.3. Porosity of the scaffolds

Further, I would like to focus on the macroscale parameters which describe the porous materials and can be directly measured or estimated.

The thickness of walls is implicitly incorporated in the term porosity, ϕ , the critical parameter of the porous structures. It defines the percentage of void space in a scaffold and can be expressed by the following equation:

$$\phi = 1 - \frac{\rho_{scaffold}}{\rho_{material}}, \quad (2.3)$$

where $\rho_{material}$ is the density of the raw material the scaffold made of and $\rho_{scaffold}$ is the apparent density of the structure and equals to the scaffold weight divided by its volume. The porosity values of the printed scaffolds were measured with the dry-weight method.

2.4. Permeability of the scaffolds

Another crucial characteristics of the biomaterials applied in the bone tissue implants is permeability. It characterises the resistance to flow through the pores and depends exclusively upon the configuration of the scaffold's void space [44].

The main issue related to measuring the permeability of porous solids is the absence of widely accepted standards to run the experiment. In our group, the permeability of the scaffolds is experimentally determined with a falling head test. Further, the theoretical background of this experiment will be explained.

It is practically impossible to fully resolve the Navier-Stokes differential equation, governing the motion of the fluid through the scaffolds. Therefore the simplified version of it — Darcy's law, neglecting inertia forces, is applied. Darcy's law links the flux q to the pressure gradient vector ∇p :

$$q = -\frac{\kappa}{\mu} \nabla p, \quad (2.4)$$

where κ is an intrinsic permeability of the medium, μ is a dynamic fluid viscosity. But this law is only valid when the flow is in a laminar regime. The dimensionless quantity used to predict the flow condition is Reynolds number, Re .

$$Re = \frac{\rho u d}{\mu}, \quad (2.5)$$

where ρ is a fluid density, u — a fluid velocity, d — a characteristic length (in our case the maximum pore size in the scaffold) and μ was already introduced as a dynamic fluid viscosity [23]. Small Reynolds number, for porous media below 10, suggests laminar flow,

while large Reynolds number corresponds to the turbulent regime when inertia forces are comparable with the viscous forces [44]. However, it should be noted that there is no sharp transitions between laminar and turbulent regimes at a particular Reynolds number and the inequality $Re < 10$ only allows us to assume that the flow is definitely laminar and the permeability coefficient κ can be estimated from Darcy's law.

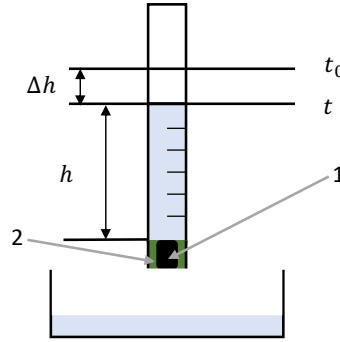


Figure 2.11: Falling head permeability test setup. 1 — sample; 2 — sample holder, silicon plug.

In the falling head experiment, the height of the water column h and time t are tracked over the course of the experiment. From the acquired data points, one can estimate the permeability of the sample through the following derivations:

$$Q = \frac{\kappa A_s \rho g h}{\mu L}, \text{ (Darcy's law)} \quad (2.6)$$

where A_s is the cross-sectional area of the sample, L — the thickness of the scaffold in the flow direction.

$$Q = A_c \left| \frac{\Delta h}{\Delta t} \right|, \text{ (law of conservation of mass)} \quad (2.7)$$

where A_c is the cross-sectional area of the column. Equating the two expressions for the total discharge Q , we get the following:

$$-A_c \frac{\Delta h}{\Delta t} = \frac{\kappa A_s \rho g h}{\mu L}, \quad (2.8)$$

the minus sign on the left side of the equation due to $\Delta h < 0$. In the limit $\Delta h/\Delta t \Rightarrow dh/dt$:

$$-\frac{dh}{h} = \frac{\kappa A_s \rho g}{\mu L A_c} dt \quad (2.9)$$

Integrating the left side over the water column height from an initial h_0 to a current h and the right one over the time from zero to t :

$$\ln \frac{h_0}{h} = \frac{\kappa A_s \rho g}{\mu L A_c} t \quad (2.10)$$

From the previous equation $\ln \frac{h_0}{h} = \alpha t$. Coefficient α equals to the slope of a straight line in the plot of $\ln h_0/h$ versus t . The permeability coefficient can be extracted from the value of α :

$$\kappa = \alpha \frac{\mu L A_c}{A_s \rho g} \quad (2.11)$$

2.5. Mechanical testing of the scaffolds

The mechanical compression test was performed on all of the 80 samples according to the ISO 13314:2011 standard [52]. LLOYD Instruments LR 5K materials testing machine with 5 kN load cell was set to 0.05 mm/s strain rate and 1 N of preload. The end criteria of the test was defined as 50% of strain \Leftrightarrow 8 mm displacement (for a few initial samples the limit was set to 44% \Leftrightarrow 7 mm displacement).

From a single experiment, the stress-strain curve of a sample can be retrieved. Proceeding with the analysis of the curve, the characteristic parameters can be determined: yield strength, elastic gradient, plateau stress. The typical look of the stress-strain curve for porous and cellular metals is illustrated in figure 2.12A. Though the material I use is resin the trend of the material behaviour under the compression is the same.

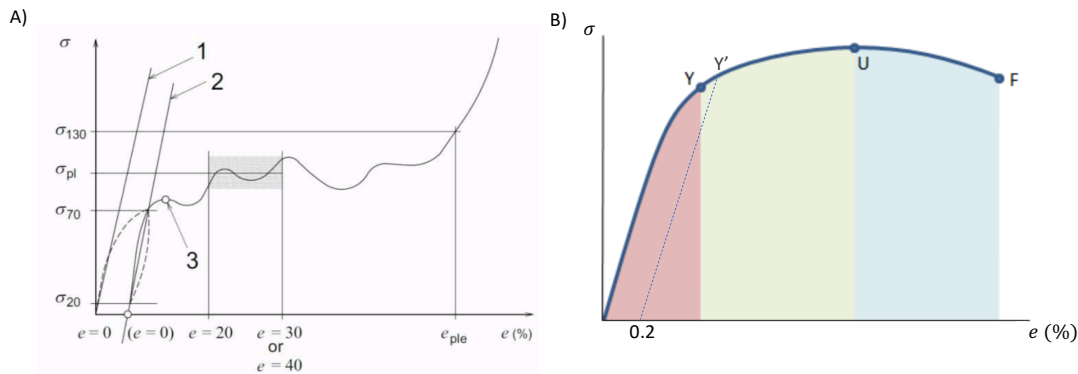


Figure 2.12: A) Stress σ as a function of strain e [27]. 1 — quasi-elastic gradient; 2 — elastic gradient; 3 — first maximum compressive strength. B) Stress-strain curve for the ductile material [2]. The yield point — Y , the offset yield point — Y' , the ultimate strength at point U , F corresponds to the fracture point.

The slope of the linear dependence between stress and strain is the elastic modulus E . The yield point in figure 2.12B defines the elastic limit of the material, the strain will be recovered after unloading. So the yield strength σ_y equals the stress value at the yield point Y . If the point is not easily defined the offset yield point Y' at 0.2% plastic strain could be used for the rough estimation. The plateau stress is a typical trend in the stress-strain curve for porous materials in contrast to solid structures. After the yield stress is reached the weakest layer of the structure collapses. While the machine continues to apply pressure at the constant strain rate, the next layers collapse in turn. This explains the observed oscillations in the curve. After all the layers deformed and the scaffold is pressed to an almost solid structure — the densification occurs. The plateau stress, σ_{pl} , is defined as the mean of the stresses between the 20% and 30% (40%) strain rate. The end of the plateau is defined as the stress at 130% of the plateau stress.

2.6. Micro-CT scanning

The morphological properties of four samples were assessed with the micro-CT scanning. It was performed on a Phoenix Nanotom scanner with the voxel size of $7.5 \times 7.5 \times 7.5 \mu\text{m}$. Top view DICOM slices were then extracted with $7.5 \mu\text{m}$ slice increment and processed in Fiji [47]. The picture on the front page of this report is a slice of one of the designed samples.

The mean and standard deviation values of the samples' wall thickness and pore size were computed using the plugin for bone image analysis BoneJ [16]. In this plugin, the thickness at a point is defined as the diameter of the greatest sphere that fits within the structure and which contains the point. In a similar way, the pore size is measured with the distinction being that the points relate to the void space. These analyses were made on a series of 800 images (image 750 — image 1550). The pre-processing consisted of cropping the images so that the void space outside the sample was removed, thresholding the images (“Auto Threshold”), followed by five iterations of a noise removal algorithm (“Despeckle”).

The Hausdorff distance filter was applied in MeshLab to the designed mesh and the one reconstructed from the micro-CT scan sample [12]. This filter measures how similar two geometries are, computing a distance metric between two meshes. The Hausdorff distance $d_H(X, Y)$ between the two subsets X and Y is defined by

$$d_H(X, Y) = \max \left\{ \sup_{x \in X} \inf_{y \in Y} d(x, y), \sup_{y \in Y} \inf_{x \in X} d(x, y) \right\} \quad (2.12)$$

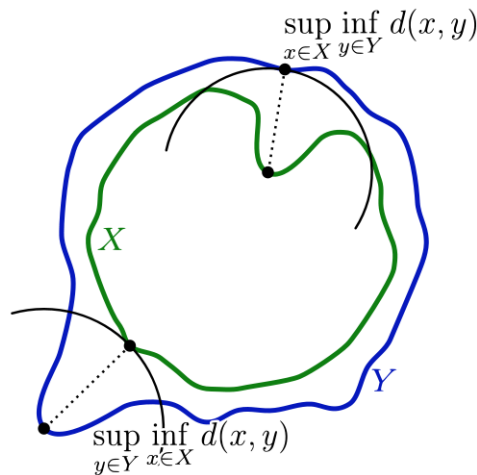


Figure 2.13: Components of the calculation of the Hausdorff distance between the green line X and the blue line Y [13]

2.7. COMSOL model

In order to predict the novel material behaviour without the necessity of printing large number of samples and conducting the experiments, the finite element modelling can be applied. To predict the fluid dynamics in the developed metamaterial, I used the finite element analysis software COMSOL [38].

In COMSOL, I developed 3D single-phase fluid flow model simulating the passage of water through the material. One of the common approaches is to simulate only the void space of the scaffold, where the fluid can go. Even this way, the simulation of the whole scaffold, consisting of 200 unit cells, is enormously computationally expensive. To create a feasible COMSOL simulation, the void domain of a single layer ($5 \times 5 \times 1$ unit cells), corresponding to each regular design, was used as an input geometry file. For the random design, each layer is different from the others, which is why this type of design was left out of focus. The regular designs also have two planes of symmetry orthogonal to each other. Consequently, only a quarter of a layer was simulated.

The geometry of the void space can be computed with the Boolean operation NOT, applied to the rectangular cuboid with the quarter layer size, $2.5a \times 2.5a \times a$, and the scaffold itself. This procedure was implemented in the SolidWorks software. The crucial parts of it are visualised in the figure 2.14, using an example of the original Schwarz P design.

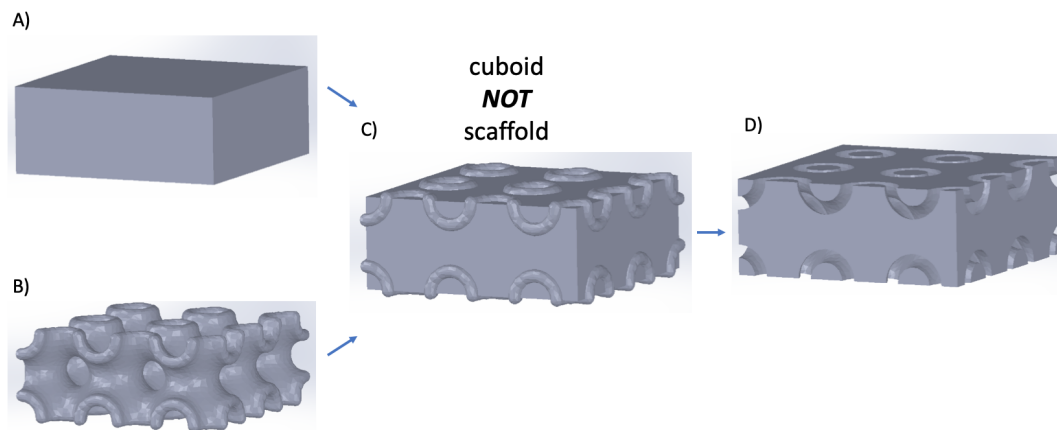


Figure 2.14: A) Solid rectangular cuboid with the dimensions of the quarter of Schwarz P layer. B) Quarter of one layer of the Schwarz P scaffold ($2.5 \times 2.5 \times 1$ unit cells). C) The rectangular cuboid and the scaffold combined. D) The void domain acquired after the Boolean operator NOT was applied to the geometry in C.

All other designs presented in the section 2.1.3 and the non-modified geometries undergone the same procedure. The mesh was exported as a *Parasolid* file for further import in COMSOL.

The model set-up and the results of the FE simulations will be presented in chapter 4, because the model tuning relied on the experimental results.

3

Results

3.1. Fabricated samples

Five samples of each design were printed, including standard surfaces without removed patches. This resulted in 80 samples in total: 30 for P surface, 25 for G and D surfaces. The picture of each type of scaffold design with the removed support is presented in the figure below.

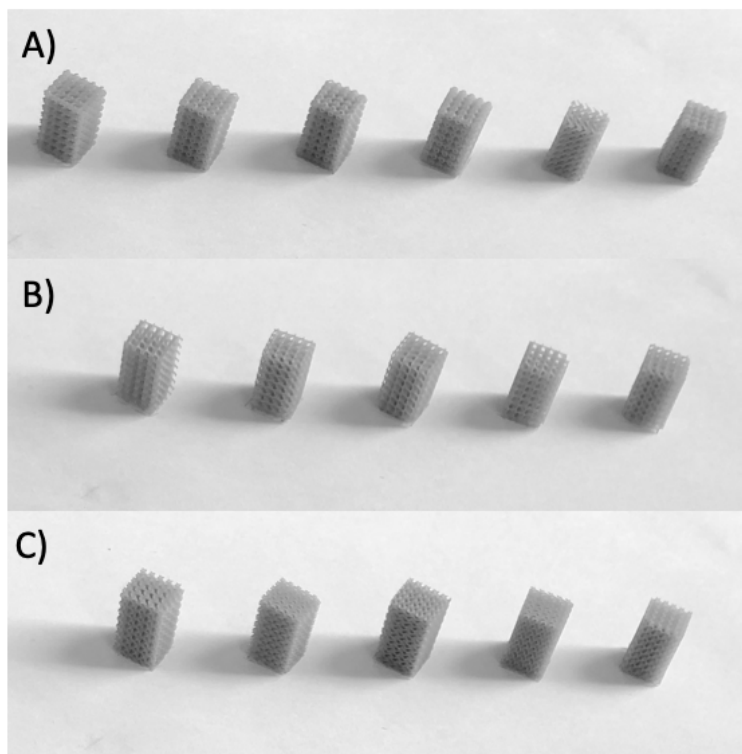


Figure 3.1: A) Schwarz P designs from left to right: without 2 hexagons, without 4 fundamental patches, normal, random, without 4 hexagons, without 6 fundamental patches. B) Schwarz D designs from left to right: without 1 hexagons, without 4 fundamental patches, normal, random, without 6 fundamental patches. C) Gyroid designs from left to right: without 2 hexagons, without 4 fundamental patches, normal, random, without 4 hexagons.

A closer look at the samples is provided in the figure 3.2:

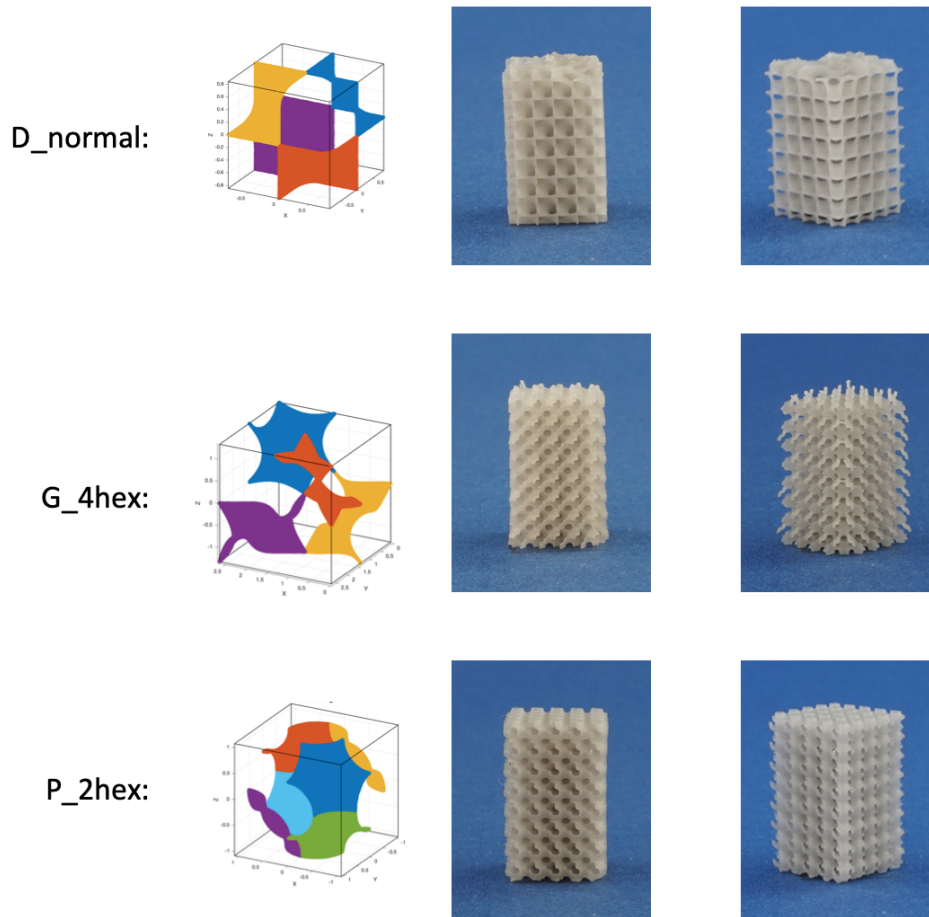


Figure 3.2: Scaffolds with Schwarz D, Gyroid and Schwarz P geometries. On the left of each row — the unit cell composing the structure.

3.2. Experimental results

In this section, I present the main experimental findings of my thesis: the results of falling head permeability test and compression test for all of the fabricated samples.

3.2.1. Permeability test results

The procedure of the falling head permeability test was previously described in the section 2.4. After fixing each sample in the setup, three identical tests in series were performed. The sample permeability was extracted from the data points and averaged over three measurements. The height of the water, h , and its velocity, u , at each time point were estimated as:

$$h = \frac{p}{\rho g}, \quad (3.1)$$

$$u = \frac{dh}{dt}, \quad (3.2)$$

where p is a pressuremeter readings, located immediately above the sample. The typical raw data plot of water height above the sample versus time is presented in the figure 3.3. Each separate peak is related to one water column going through the sample.

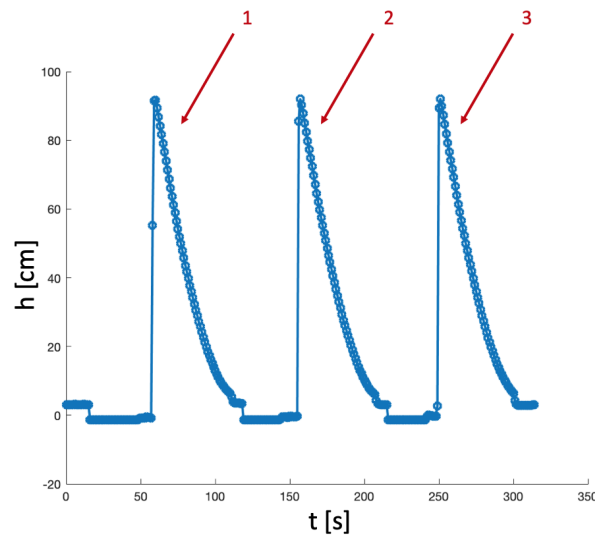


Figure 3.3: An experiment data retrieved after three consecutive experiments on the Schwarz P surface sample. The data is discrete due to 1 s time resolution of the data acquisition system.

From the equation 2.11 it follows that the sample permeability is proportional to the slope of a straight (in theory) line on the graph $\ln h_0/h$ vs t . In practice, the dependency of the variable $\ln h_0/h$ on time during the experiment is not linear. This is a result of turbulent flow at the beginning of a test when the water pressure is relatively high. With water going through the sample, the pressure drops and the flow regime switches to laminar, with the previously derived equations being applicable for permeability estimation. Thus only the data points with Reynolds number less than 10 were selected for calculations, which were the data points at later stages of the test.

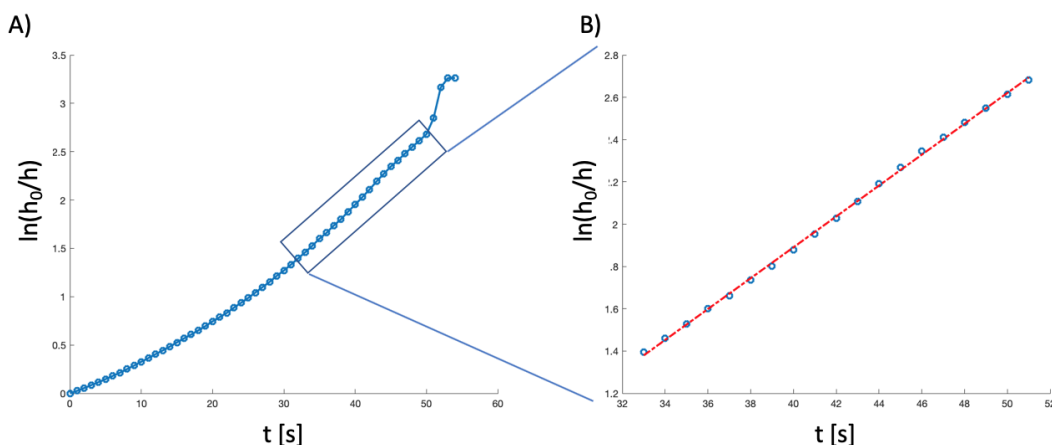


Figure 3.4: A) $\ln h_0/h$ vs time for Schwarz P sample test 1, figure 3.3. B) Part of the graph where the water flow is in laminar regime ($Re \leq 10$). The red dashed line is a linear fit of the data points.

In the figure 3.4B the slope of the dashed line corresponds to the parameter α from the equation 2.11. The permeability of the sample, extracted from the slope, was averaged over the three tests.

In a similar way, all the samples were measured, and an average and standard deviation for the permeability coefficients κ of each scaffold design were computed. Results are summarised in the table 3.1.

Table 3.1: Experimental permeability coefficients, κ , for the developed scaffolds. Each cell represent the average value, μ , and the standard deviation, σ . The units of the coefficient are $1e-9 m^2$.

	normal	1 hex.	2 hex.	4 hex.	4 fund. patches	6 fund. patches	random
P	1.527 (0.092)	—	1.816 (0.054)	3.463 (0.310)	2.200 (0.041)	2.173 (0.051)	1.992 (0.061)
D	2.154 (0.044)	2.546 (0.088)	—	—	2.061 (0.040)	2.204 (0.047)	2.593 (0.051)
G	0.716 (0.080)	—	1.007 (0.054)	1.678 (0.028)	1.185 (0.062)	—	1.351 (0.055)

To determine if there is a statistically significant difference between the measured permeability values, Student's t-test was applied. The t-test evaluates the difference between the means of two groups taking into account the number of samples in each group and their standard deviation. This test was applied pairwise to each group of samples with P, D, G geometry separately. As the number of samples in each group was the same, and the sign of the difference is irrelevant, the two-tailed Independent t-test was used. In the Independent t-test the t-value is calculated by the following formula [15]:

$$t - value = \frac{\mu_1 - \mu_2}{\sqrt{\frac{(n_1-1)\sigma_1^2 + (n_2-1)\sigma_2^2}{n_1+n_2-2}} \cdot \sqrt{\frac{1}{n_1} + \frac{1}{n_2}}} \quad (3.3)$$

where μ_1 and μ_2 are average values of the sample sets, σ_1 and σ_2 — variances, n_1 and n_2 — number of data points in each set. Calculated p-values are presented in the appendix B, the ones related to the permeability data are presented in the tables B.1 — B.3. The significance level was set to 0.05.

3.2.2. Mechanical test results

In the figure 3.5, the mean compression graphs of the 80 samples with 95% confidence interval (CI) are displayed. The CI was calculated with the following formula:

$$CI = \mu \pm 1.96 * \frac{\sigma}{\sqrt{n}}, \quad (3.4)$$

in which μ is a mean stress value over the $n = 5$ samples, σ is a standard deviation.

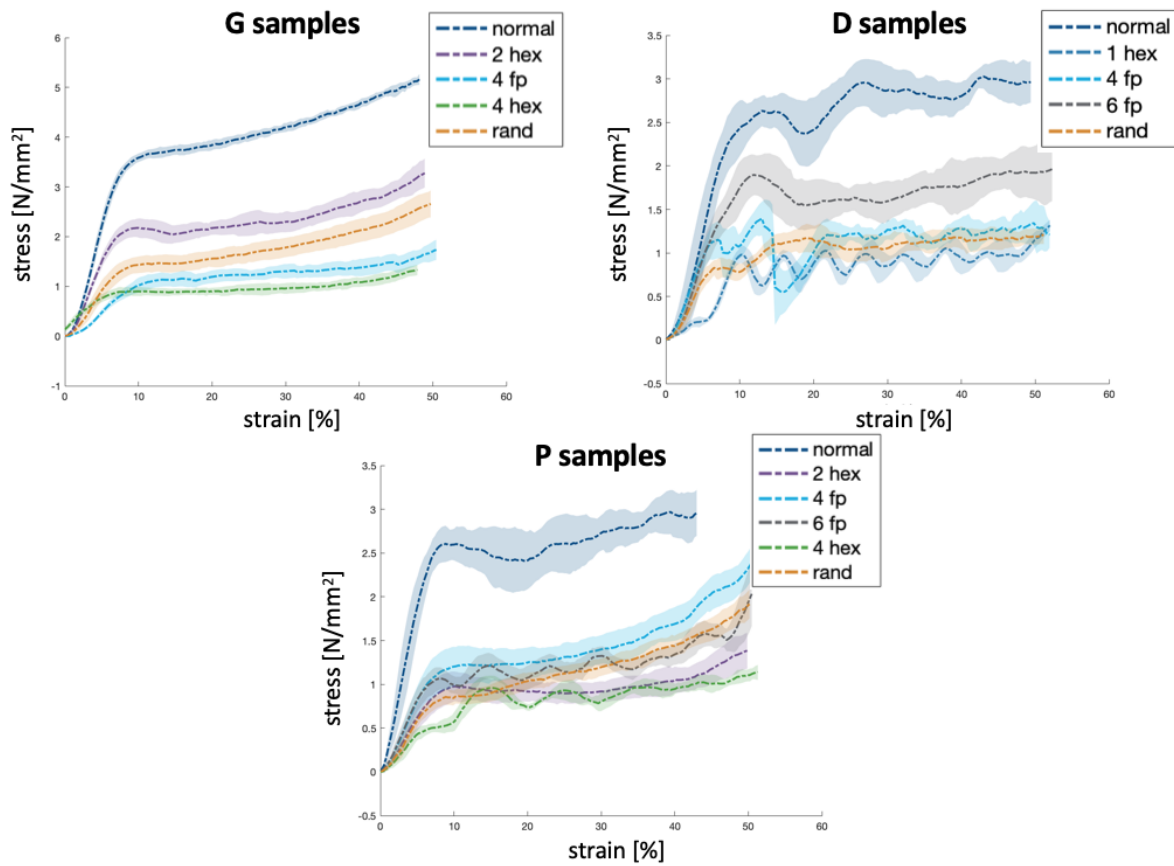


Figure 3.5: Mean stress-strain curves with 95% confidence intervals.

As can be seen in figure 3.5, there is an evident difference in the elastic region between classic and modified geometries for all design groups. G samples showed much less wavering in the plateau region than D and P scaffolds. At the same time, the densification occurred in all the scaffolds.

From stress-strain curves characteristic parameters, previously mentioned in section 2.5, were extracted: elastic gradient, yield stress and plateau stress. The mean and standard deviation values were calculated for each design and gathered in the table 3.2. To define whether the mechanical parameters of each design group are statistically different, the two-tailed t-test was applied. The results of the test are summarized in the appendix B, tables B.4 — B.12.

Table 3.2: A combined table of permeability and compression test results.

Surface	Design	Permeability	Elastic gradient	Yield stress	Plateau stress
		$10^{-9} m^2$	<i>MPa</i>	<i>MPa</i>	<i>MPa</i>
P	normal	1.527 (0.092)	35.241 (4.319)	2.261 (0.193)	2.585 (0.095)
	2 hexagons	1.816 (0.054)	12.867 (2.862)	0.854 (0.187)	0.940 (0.146)
	4 hexagons	3.463 (0.310)	10.796 (2.924)	0.485 (0.067)	0.886 (0.051)
	4 fund. patches	2.200 (0.041)	17.379 (4.761)	1.048 (0.262)	1.418 (0.193)
	6 fund. patches	2.173 (0.051)	17.312 (2.178)	0.968 (0.140)	1.218 (0.118)
	random	1.992 (0.061)	14.070 (2.130)	0.726 (0.118)	1.217 (0.122)
D	normal	2.154 (0.044)	36.309 (7.734)	2.265 (0.371)	2.796 (0.280)
	1 hexagon	2.546 (0.088)	6.598 (1.261)	0.189 (0.065)	0.922 (0.126)
	4 fund. patches	2.061 (0.040)	22.190 (2.837)	1.115 (0.259)	1.205 (0.061)
	6 fund. patches	2.204 (0.047)	24.194 (5.937)	1.573 (0.415)	1.658 (0.209)
	random	2.593 (0.051)	17.210 (1.173)	0.790 (0.129)	1.102 (0.130)
G	normal	0.716 (0.080)	54.969 (2.984)	3.076 (0.057)	4.225 (0.090)
	2 hexagons	1.007 (0.054)	33.611 (3.956)	1.928 (0.181)	2.359 (0.221)
	4 hexagons	1.678 (0.028)	13.148 (2.107)	0.734 (0.081)	0.953 (0.111)
	4 fund. patches	1.185 (0.062)	13.057 (1.266)	0.940 (0.194)	1.287 (0.146)
	random	1.351 (0.055)	21.751 (3.797)	1.236 (0.159)	1.804 (0.229)

The photos of the samples after the compression test are presented in the appendix C. The failure modes were similar for matching designs. For instance, the asymmetrical designs, like *G without 2 hexagons*, *P without 2 hexagons* and *D without 1 hexagon*, were collapsing in the direction of the removed hexagons, figure 3.6.

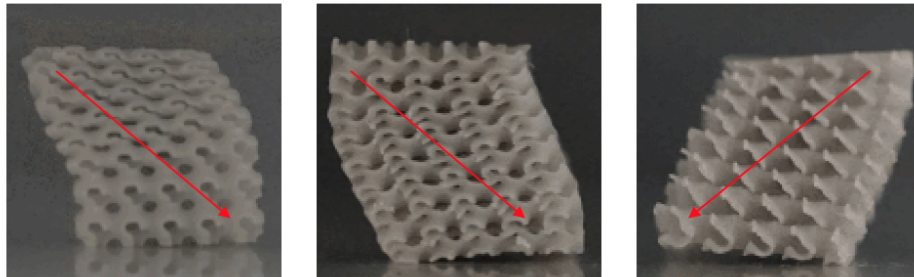


Figure 3.6: From left to right: pictures of the *P without 2 hexagons*, *G without 2 hexagons* and *D without 1 hexagon* scaffolds after the compression test.

The other designs, except random ones, preserved the symmetry of the original unit cell and failed layer by layer without displacement in a horizontal direction, figure 3.7.

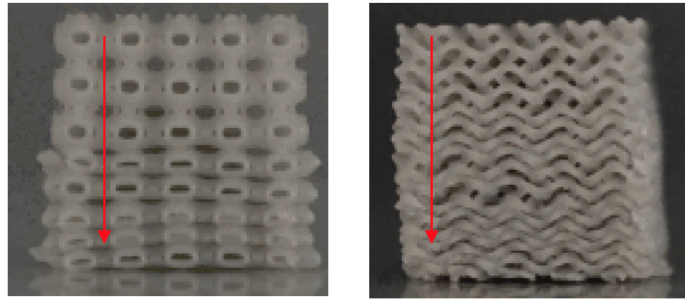


Figure 3.7: From left to right: pictures of the P and G designs *without 4 fund. patches* after the compression test.

The previous figure does not include the picture of *D without 4 fund. patches* scaffold, because the structure was found to be excessively brittle and lost structure under the compression as shown in figure 3.8. It also applies to other designs from the D group, except the one *without 1 hexagon*. Surprisingly, this design improved the mechanical performance of the structure.

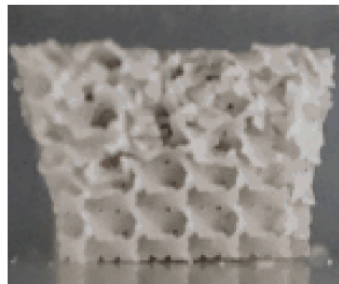


Figure 3.8: Picture of the D design *without 4 fund. patches* after the compression test.

3.2.3. Relation between porosity and physical properties

Microstructural morphology of porous materials can not be characterised with one macroscale parameter. Thus permeability and mechanical properties can not be accurately predicted without conducting an experiment or running a simulation. However, macro parameter porosity ϕ is considered to be a valid one while noting the efficiency of the raw material utilisation.

In figures 3.9 — 3.11 permeability, elastic gradient and yield stress are plotted against the porosity. The mean dry-weight porosity values of the scaffolds are specified in the table A.1. For clarity, correspondence between the abbreviations used in the graphs and the unit cells' geometry is provided.

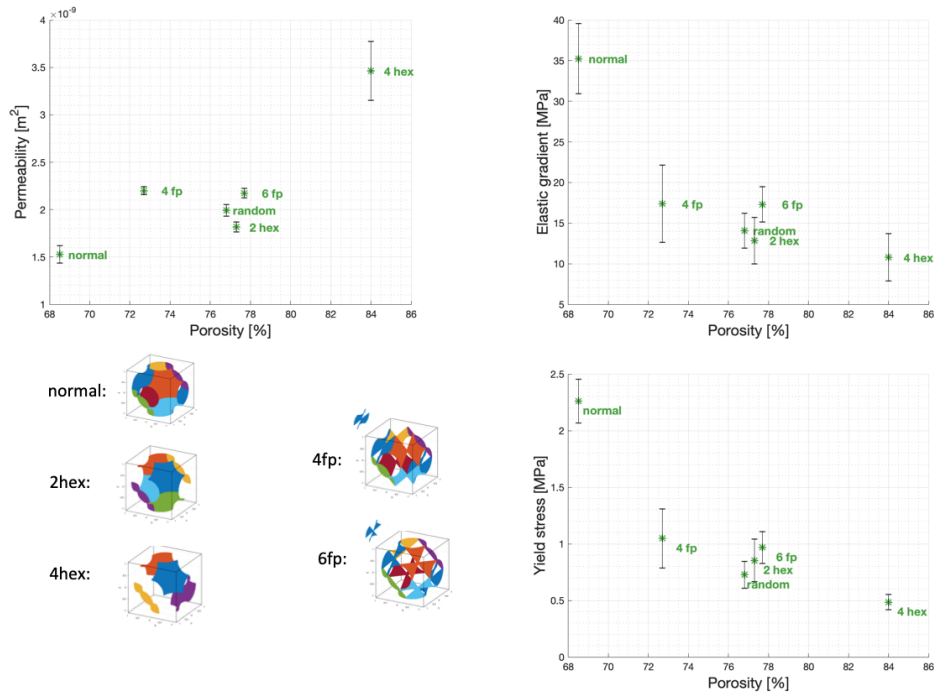


Figure 3.9: Scatter plot with the mean parameter values and the error bars set to standard deviation of the Schwarz P designs.

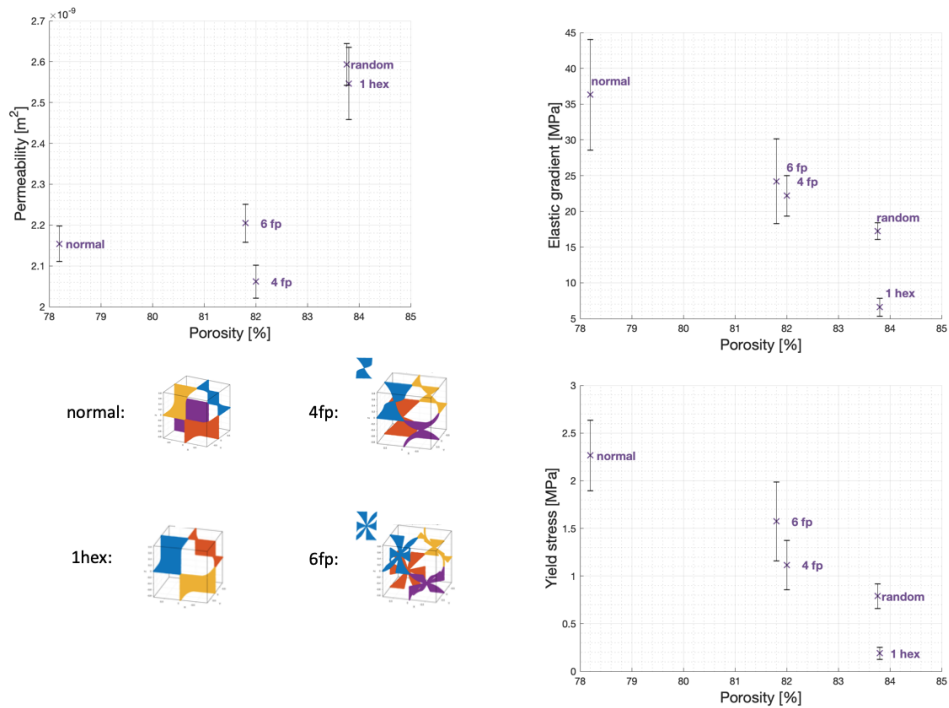


Figure 3.10: Plots of the Schwarz D designs.

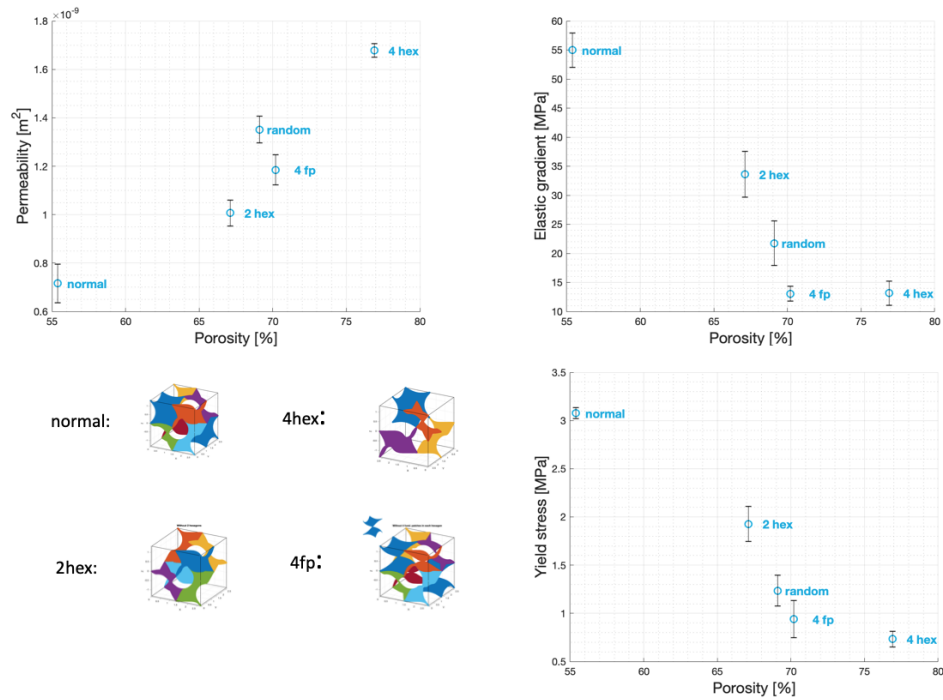


Figure 3.11: Plots of the Gyroid designs.

In most of the graphs, the correlation between the physical properties and porosity is disrupted from a linear trend. Since in some cases more porous scaffolds have lower permeability or more stiff. It suggests that artificially introduced channels in the scaffolds not only increase the porosity but also significantly affect the topology of the surface and consequently, the physical parameters of the scaffolds. Noteworthy, the design *D without 4 fund. patches* had a little lower permeability than the non-modified one.

To visualise how the characteristics of the samples from different surface groups relate to each other, I plot combined permeability, elastic gradient and yield stress. From the figures 3.12 — 3.14 it can be concluded that the overall linear trend does not prove to be a good model for the designed samples.

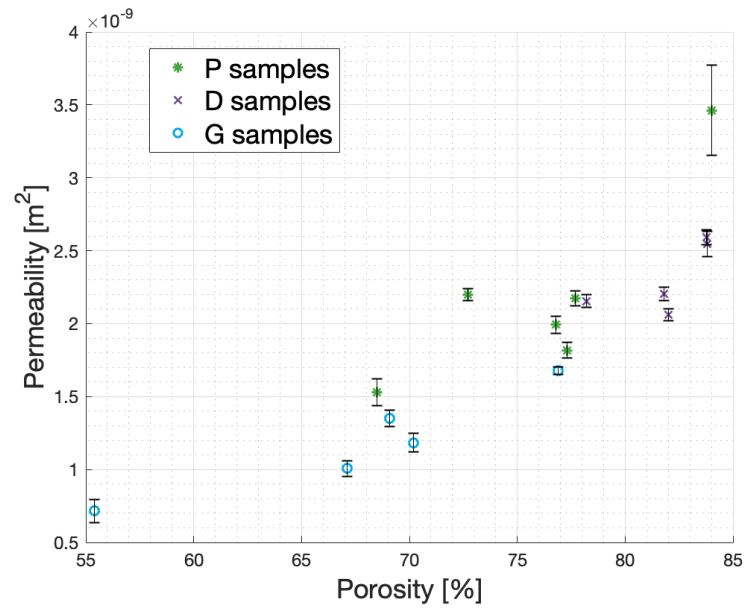


Figure 3.12: Combined permeability values of the Schwarz P, Schwarz D and Gyroid sample groups versus porosity.

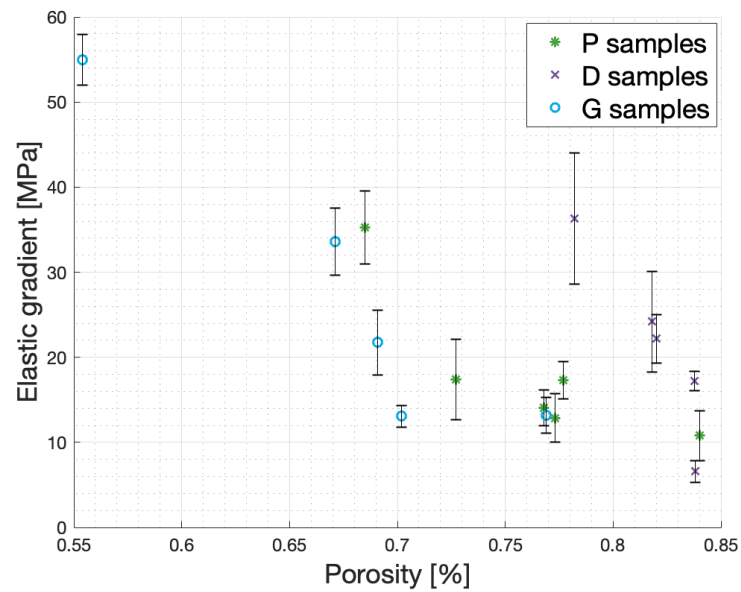


Figure 3.13: Combined elastic gradient values of the Schwarz P, Schwarz D and Gyroid sample groups versus porosity.

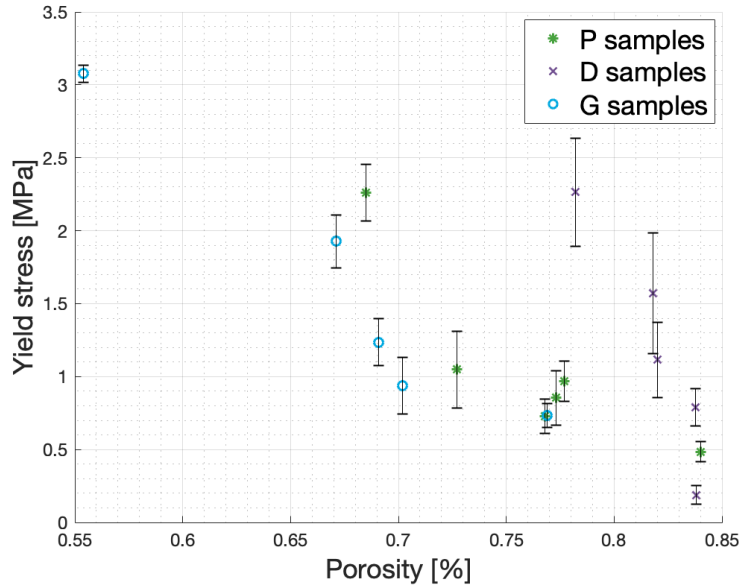


Figure 3.14: Combined yield stress values of the Schwarz P, Schwarz D and Gyroid sample groups versus porosity.

The absence of the clear trend in the previous graphs can be attributed to the significantly altered morphology of the modified scaffolds with the material removed. To quantify the dependence between the permeability and porosity, elastic gradient and porosity, yield stress and porosity for the scaffolds, the Pearson correlation coefficients were computed, table 3.3.

Table 3.3: Pearson correlation coefficients.

	Permeability	Elastic gradient	Yield stress
Porosity	0.87	-0.72	-0.73

Tradeoff between permeability and mechanical properties: it is clear that by removing fundamental patches from the unit cell, the permeability of the samples can be increased while the stiffness and yield strength will inevitably deteriorate. To quantify this interdependence, I compute the ratio of the parameters, corresponding to the altered and original structures. I assume these parameters to be statistically independent, thus the mean value and the variance of the ratios are determined as follows:

$$E(X/Y) = E(X)E(1/Y), \quad (3.5)$$

$$\text{Var}(X/Y) = E(X^2)E(1/Y^2) - E(X)^2E(1/Y)^2, \quad (3.6)$$

Applying the formulae to the collected data, the percentagewise ratios of permeability and elastic gradient values were separately estimated.

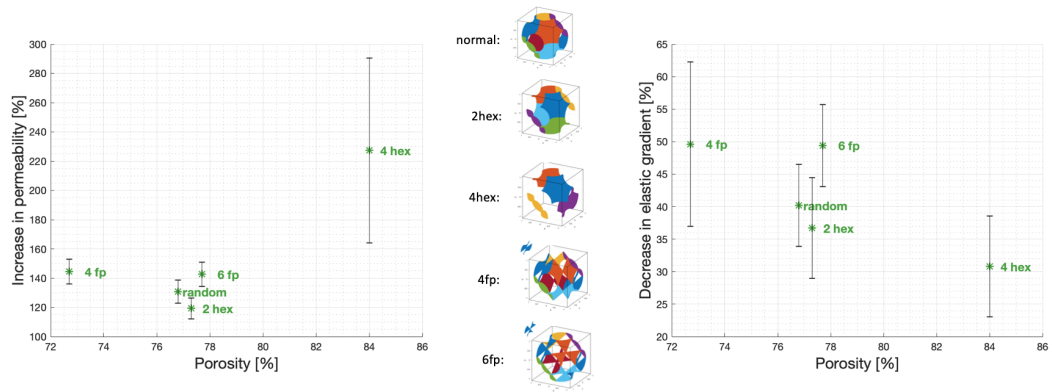


Figure 3.15: Schwarz P samples group. Percentagewise permeability (left) and elastic gradient (right) ratios of the modified scaffolds relative to the normal one (with the original unit cell).

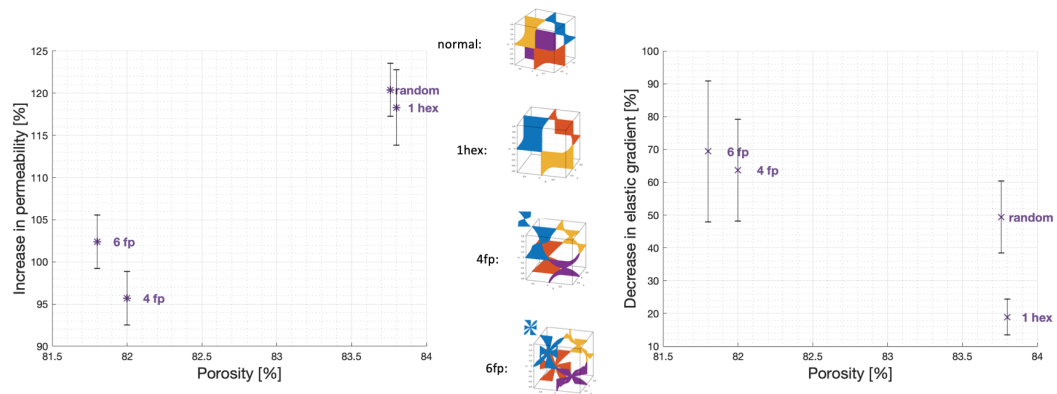


Figure 3.16: Schwarz D samples group. Percentagewise permeability (left) and elastic gradient (right) ratios of the modified scaffolds relative to the normal one (with the original unit cell).

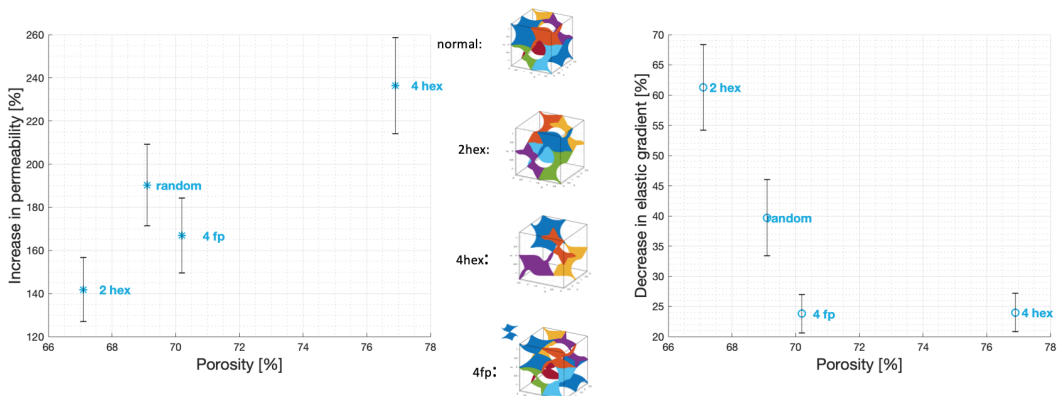


Figure 3.17: Gyroid samples group. Percentagewise permeability (left) and elastic gradient (right) ratios of the modified scaffolds relative to the normal one (with the original unit cell).

3.2.4. Micro-CT scan results

To assess the quality of the 3D printed samples, four scaffolds were subjected to micro-CT scanning. With help of the image processing program, ImageJ with BoneJ plugin, stacks of the produced images were analysed and the critical parameters retrieved [16, 47]. First of all, the mean thickness of the walls and the mean pore size were measured, as displayed in table 3.4.

Table 3.4: Micro-CT scan data.

Design	Wall thickness [μm]		Pore size [μm]	
	<i>mean (SD)</i>	<i>max</i>	<i>mean (SD)</i>	<i>max</i>
P without 4 fp	322 (64)	579	1192 (327)	1917
P without 6 fp	291 (62)	468	1175 (321)	1532
D without 4 fp	262 (57)	521	1343 (216)	1816
G random	282 (50)	541	629 (96)	961

From the table above it is clear that all of the samples had higher thickness than the design value of 200 μm . This could be explained by the imperfections in the printing and postprocessing steps during the fabrication. Moreover, the location of the sample on the printing plate influenced the printing quality, as clearly observed from the wall thickness of the two P samples, fabricated in one batch. As the thickness was determined to vary significantly between samples and it was not feasible to scan all 80 of them, for the simulations I used the designed thickness value. The mean pore size values significantly exceeded the critical value of 300 μm . It is explained by the performance of the analysing algorithms, which compute the thickness of the background at each pixel of the image and not the critical pore diameter, the diameter of the largest sphere that can freely pass through a porous medium. Though there is no clear guidance on how to define pore size in the porous medium, the critical diameter was shown to correlate well with the permeability [40].

To explore the printing quality further, the 3D structure of one of the samples (*D without 4 fundamental patches*) was reconstructed. In the figure below the mismatch between the designed structure and 3D printed one is clearly visible and the gap between the meshes grows toward the top of the sample.

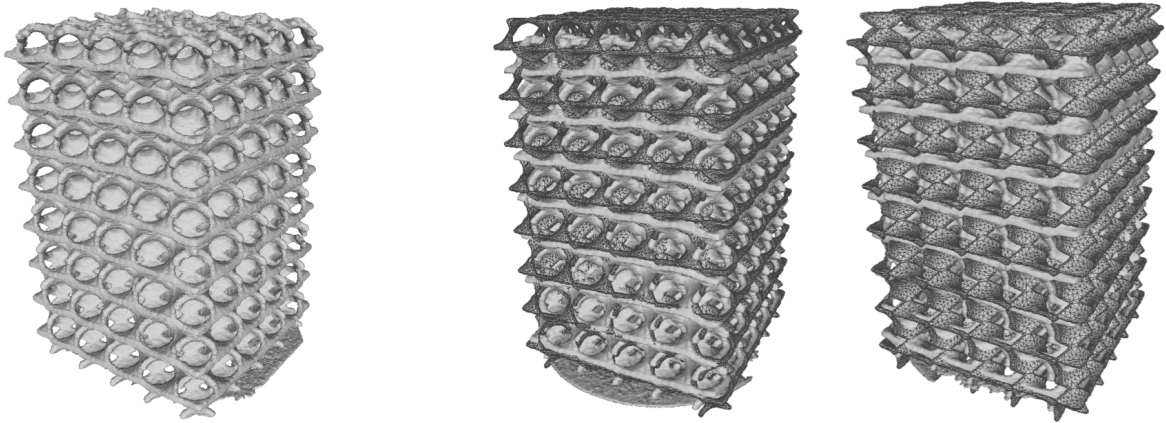


Figure 3.18: On the left the reconstructed image of the scaffold from the micro-CT scan. On the right two views of the original design (meshed one) aligned with the reconstructed scaffold.

In MeshLab one-sided filter is applied, *i.e.* $d = \sup_{x \in X} \inf_{y \in Y} d(x, y)$. Basically, for a set of points x from a mesh X (reconstructed sample) the software searches the closest point y on a mesh Y (design) to determine the Hausdorff distance. For the visualisation, computed distance is represented in colourscale for each point, see figure 3.19. The mean error between the meshes was $171 \mu m$, with the maximum of $1167 \mu m$. In the figure 3.19 the clamping of 1% was applied to prevent almost uniformly coloured mesh since only for a few points the gap reaches the maximum value.

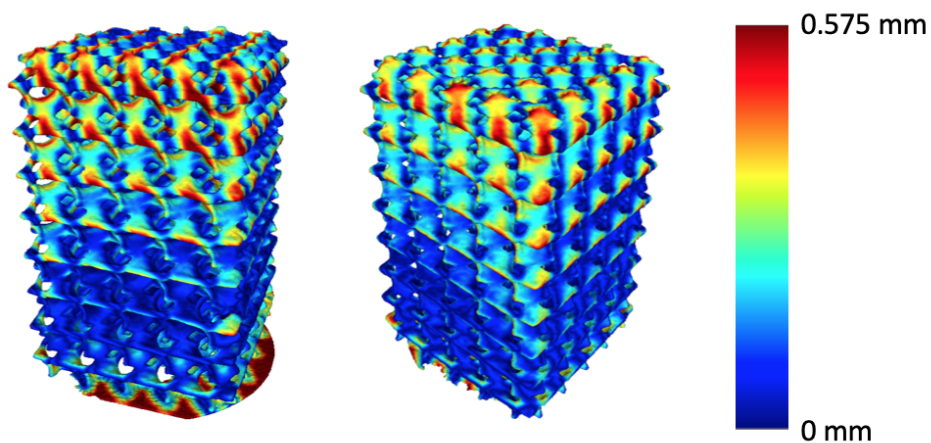


Figure 3.19: Hausdorff distance filter applied to the reconstructed sample. The distance between the meshes was linearly projected to the red-green-blue colormap.

4

Fluid dynamics simulation: tuning model and results

4.1. COMSOL model

To set up a valid model in COMSOL, a sequence of crucial decisions had to be made. I will justify all of them in the subsequent subchapters describing each part of the model.

4.1.1. Mesh

Created *Parasolid* files with the void domain geometry were imported in COMSOL and meshed with tetrahedral elements. The size of the elements was set to *Extra coarse*.

The mesh element type and the size directly affect the computation of a problem: how long it takes a model to solve, the amount of memory required and how accurate the solution is. Naturally, the time needed for the solver to converge to the solution goes up with the decrease of the element size. Thus the mesh convergence study should be performed to be confident in the accuracy of the simulation data. To do that one of the models was run with finer mesh (*extra coarse, coarser, coarse* and *normal*). The dependence of permeability values on the maximal element size in the mesh is presented in the figure 4.1.

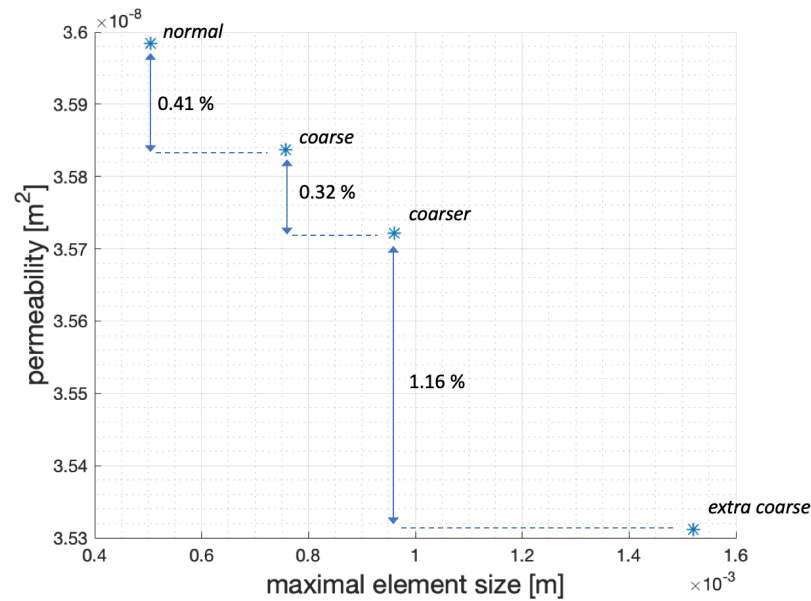


Figure 4.1: Mesh convergence study of the Schwarz P without 4 hexagon design. The values in the graph correspond to the relative difference in permeability for two meshes.

Since the difference in the permeability coefficient was negligible, the *Extra coarse* mesh size (maximum element size 0.00151 m) was found to be a reasonable choice for optimisation of simulation time.

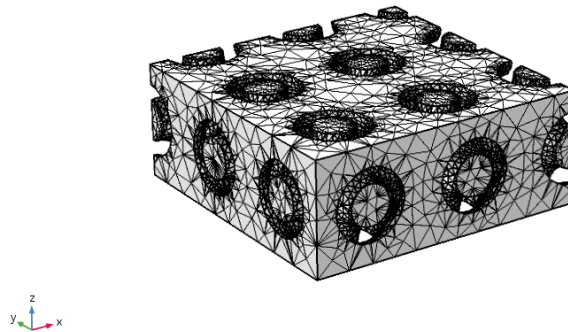


Figure 4.2: Tetrahedral mesh of the void domain of Schwarz P scaffold

4.1.2. Physics

The governing physics laws in the model were set to the single-phase creeping flow interface. Single-phase regime was chosen because the model describes only the water flow. The reasoning behind the creeping flow regime is more complex. COMSOL can solve equations derived from the Navier-Stokes equations suitable for different flow patterns: creeping, laminar, turbulent. Though the Darcy law was determined empirically, it can be shown

that, by ignoring the inertial terms in the governing equations, the Darcy law can be derived from the Navier-Stokes equation [23]. In figure 3.4, the experimental data shows that with time when the flow through the sample stabilises, the data points follow the Darcy law trend. In COMSOL, only the creeping flow equation does not cover inertia effects, thus the flow regime was set to this one and not laminar. The inlet pressure equalled 1 Pa , though the specific value is not critical due to the linear proportionality between the flux and pressure drop according to the equation 2.4. The outlet pressure was 0 Pa .

4.1.3. Boundary conditions

I have already mentioned that the computation time could be reduced by benefiting from the symmetry of the designs. In figure 4.3 C the planes, where the symmetry boundary conditions (BC further) were applied, are highlighted. The inlet and outlet faces with assigned pressure are illustrated in figure 4.3 A. The pressure drop $p_{inlet} - p_{outlet}$ was set to 1 Pa . The remaining part of the boundary was defined as wall BC with a no slip option, figure 4.3 B. This way at the solid-fluid interface the fluid velocity dropped to zero and the friction effects at the walls were reproduced in the model.

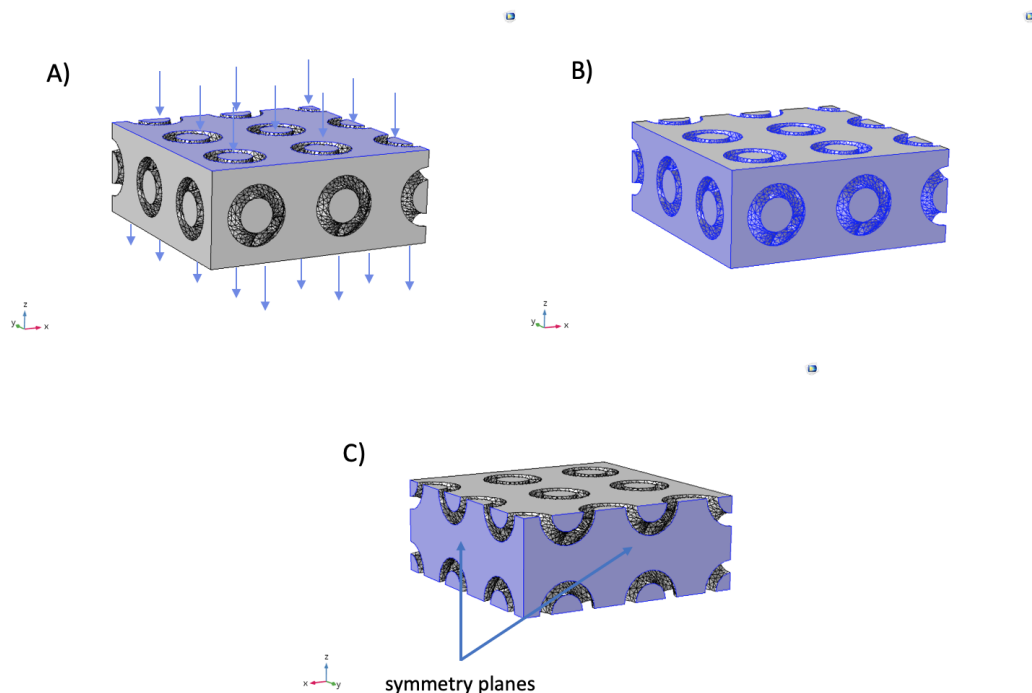


Figure 4.3: A) Inlet and outlet faces. B) Wall BC. C) Symmetry BC.

4.1.4. Study

To assign the study to the model, the choice should have been made between stationary and time-dependent studies. In case of a steady flow, the first one is applicable. But if the time of the measurement is less than the time needed for flow stabilisation the solver should be time-dependent.

To estimate the time needed for the flow to enter the stationary regime after opening the valve, I applied the following derivations to the simplified model. I assume the sample to be a hollow tube with the diameter of the characteristic pore size, $d = \frac{a}{2} = 1 \text{ mm}$, and length of the sample size parallel to the fluid flow, $l = 16 \text{ mm}$.

For laminar fluid flow, the Bernoulli's equation takes the following form [50]:

$$H_0 + l = \frac{32\mu l v}{\rho g d^2} + \frac{l}{g} \frac{dv}{dt}, \quad (4.1)$$

where H_0 is a water column height over the sample. In the stationary regime $dv/dt = 0$ and $v = \frac{\rho g d^2}{32\mu l} (H_0 + l)$ correspondingly. Transforming the equation 4.1 to the first order linear differential equation form:

$$\frac{dv}{dt} + \alpha v = \beta, \quad (4.2)$$

where $\alpha = \frac{32\mu}{\rho d^2}$ and $\beta = \frac{(H_0+l)g}{l}$. With an initial condition $t = 0$, $v = 0$ the solution of the equation takes the following form:

$$v = \frac{\rho g d^2 (H_0 + l)}{32\mu l} (1 - e^{-\alpha t}) \quad (4.3)$$

From the velocity-time dependence, the characteristic time of flow setting is $\frac{32\mu}{\rho d^2} \simeq 0.03$ seconds. For this time period, the level of water drops by 0.4 mm approximately, which negligibly small in our experiments. The flow velocity $dh/dt \simeq 0.013 \text{ m/s}$ was estimated from Reynold's number formula with $Re = 10$. So the flow can be assumed to be stationary.

4.2. Results

Using the postprocessing tools within COMSOL, flow velocity field and fluid shear stress on the walls can be visualised. The estimation of the permeability was also set within the model and based on Darcy's law.

4.2.1. Velocities distribution

In the figures 4.4 — 4.6 flow velocity field is presented. Due to the presence of two symmetry planes, the flow distribution over the whole layer can be estimated by mirroring the simulation results of the quarter. In figure 4.4 it is shown for the Schwarz P geometry.

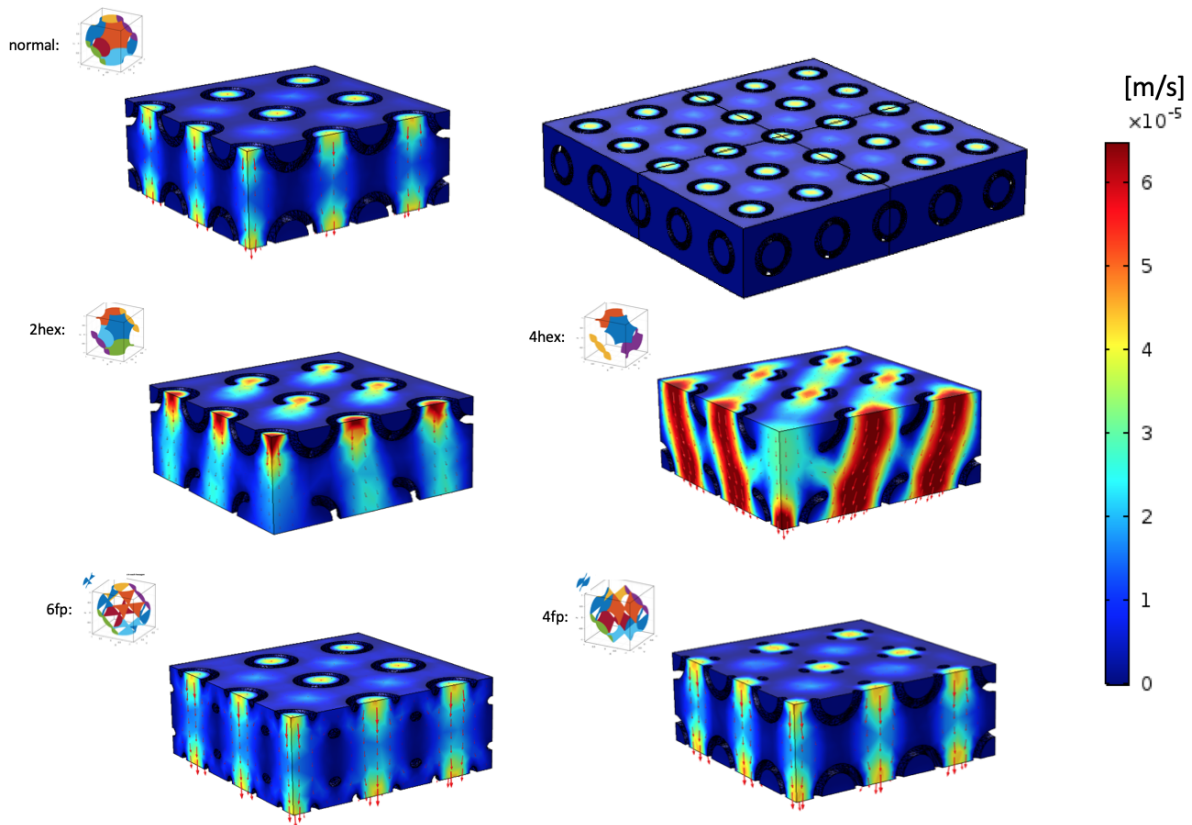


Figure 4.4: Results for the designs with Schwarz P structure. Velocity magnitude colour plot with a red arrow plot representing the orientation of the flow through the scaffold. Next to each sample — a unit cell geometry.

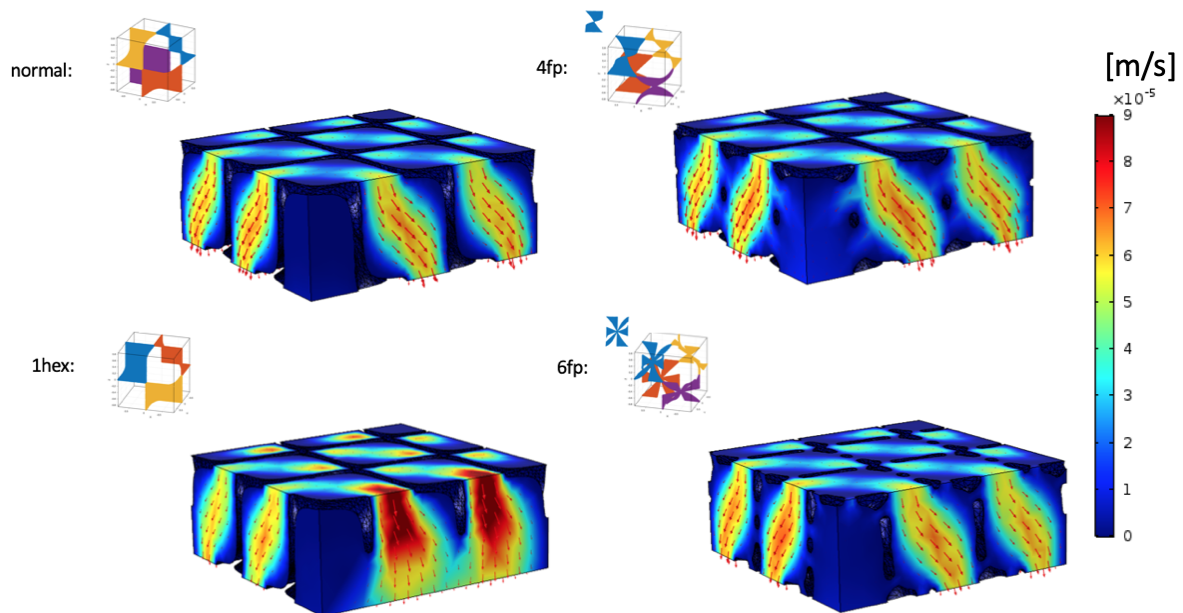


Figure 4.5: Results for the designs with Schwarz D structure.

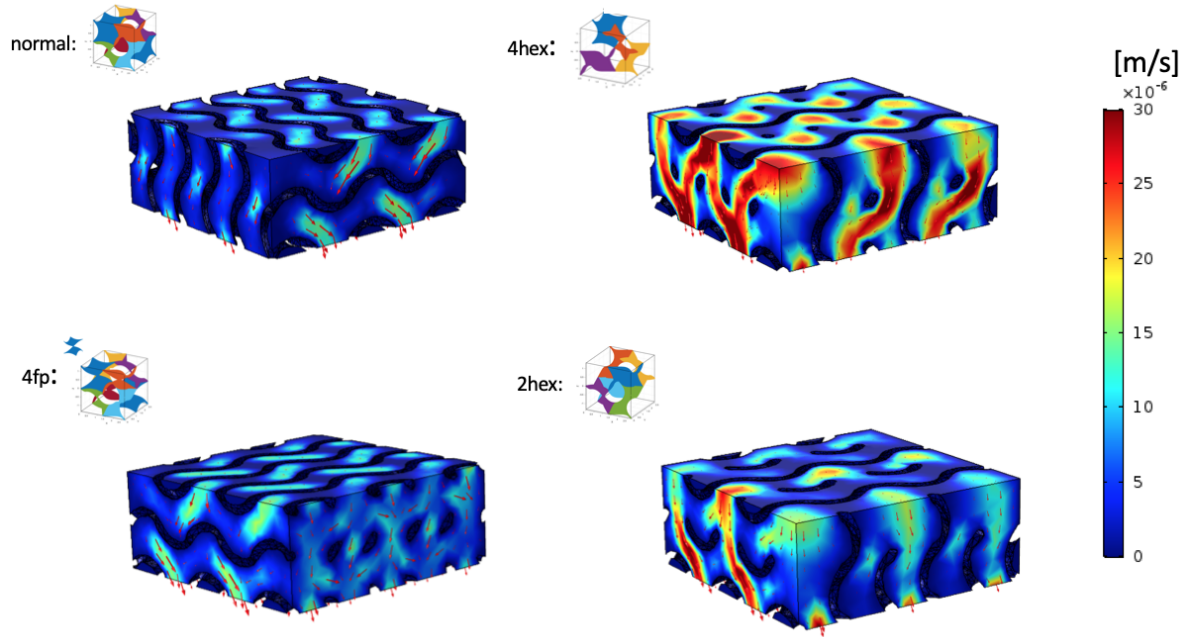


Figure 4.6: Results for the designs with Gyroid structure.

From the velocity distribution fields for all samples groups, the fluid flow rate was higher for the designs with bigger pores introduced (removed whole hexagons). The velocities in the Schwarz D group exceeded the others, while Gyroid scaffolds had the lowest flow speed. The velocity profiles of the designs *without 4 or 6 fundamental patches* are visually similar to the original ones, the designs *without 1, 2 or 4 hexagons* significantly disturbed the flow.

4.2.2. Wall shear stresses

Wall shear stress, τ_{wall} , is defined as the tangential force per unit area that is exerted by the flowing fluid on the surface of the scaffold. The magnitude of the wall shear stress is calculated in COMSOL by the following equation:

$$\tau_{wall} = \mu\gamma_{wall}; \quad (4.4)$$

where μ is the fluid dynamic viscosity and γ_{wall} is the wall shear rate, equals to the velocity gradient near the wall. In the figures 4.7 — 4.9 wall shear stress on the walls of the designed scaffolds are presented. For visualisation purposes, the colour range was constricted. The total shear force, F_{total} , and the average value of the computed shear stress is specified for each design. F_{total} is defined as an integral of shear stress τ_{wall} over the surface.

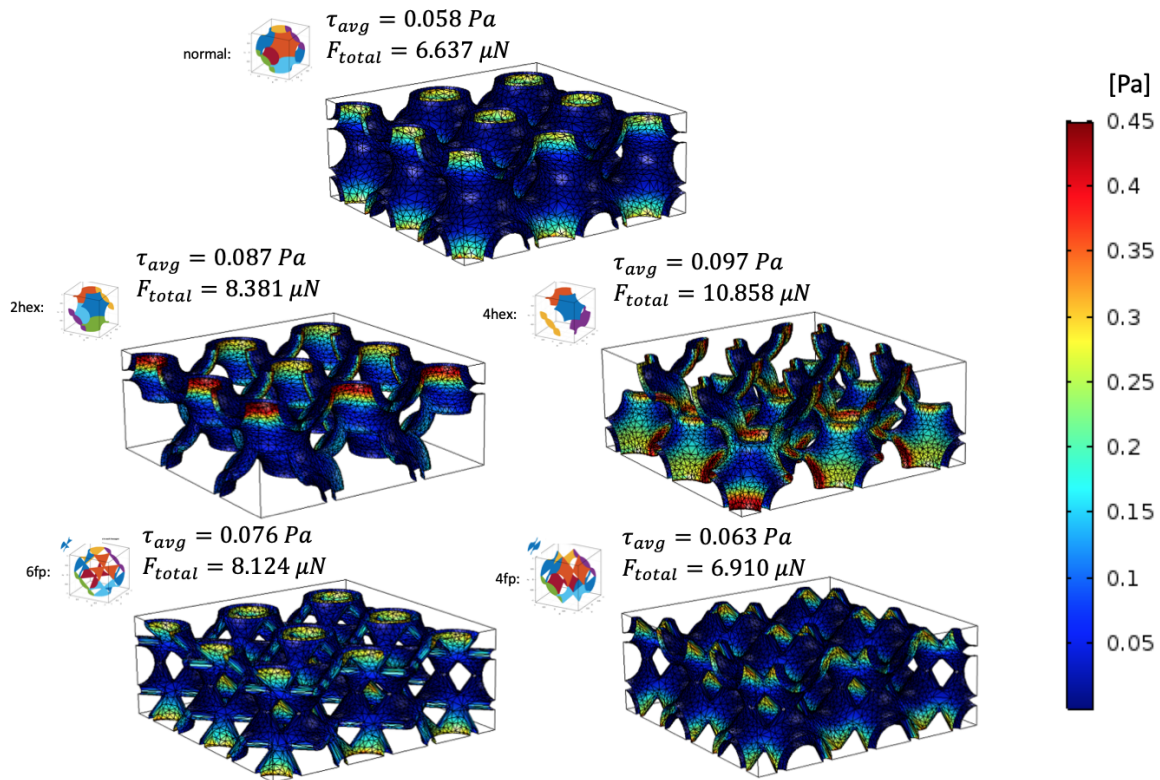


Figure 4.7: Wall shear stress of the Schwarz P scaffolds.

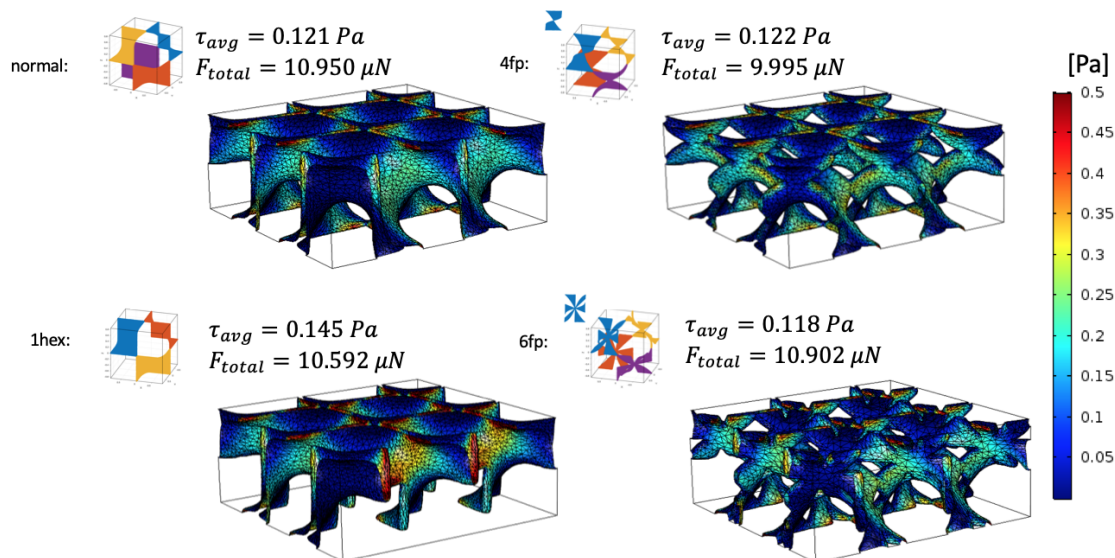


Figure 4.8: Wall shear stress of the Schwarz D scaffolds.

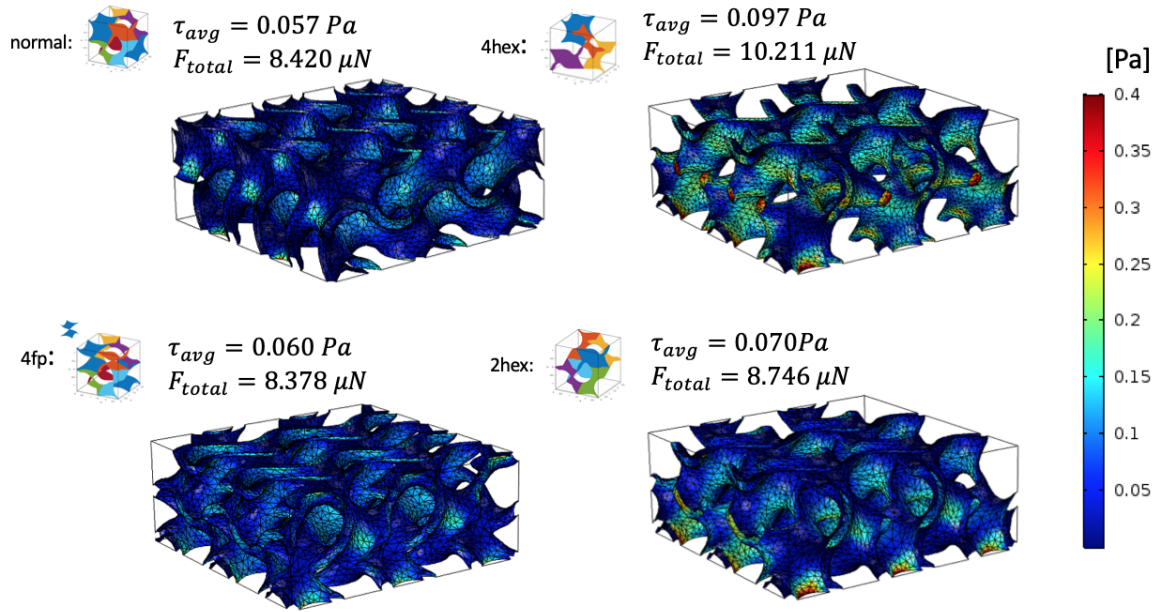


Figure 4.9: Wall shear stress of the Gyroid scaffolds.

According to the COMSOL estimation, shear stresses were higher in the designs with faster flow. In agreement with the velocity fields, the designs with the removed hexagons exhibited higher average shear stresses, τ_{avg} , on the walls than the designs with smaller parts removed or non-modified ones. Though the total shear forces diverged from this trend.

4.2.3. Permeability values

With the permeability coefficients, the porosity and specific surface area values were also computed in COMSOL. These two extra parameters are considered to influence the transport of fluids within scaffold [44]. The semi-empirical Kozeny equation expresses the relation between permeability, κ , porosity, ϕ , and specific surface area, s [53]:

$$\kappa = \frac{1}{c_K} \frac{\phi^3}{s^2}, \quad (4.5)$$

where c_K is the empirical Kozeny constant, which is strongly related to the geometry of pores and can not be estimated in advance. The permeability values predicted by the model are presented in the plots permeability, κ , versus Kozeny factor, ϕ^3/s^2 . The slope of the line, linearly fitting the data points, equals to the Kozeny constants, c_K . The coefficients of determination, R^2 , measuring the percentage of the permeability variation that is explained by a linear model, was also extracted and added to the figures.

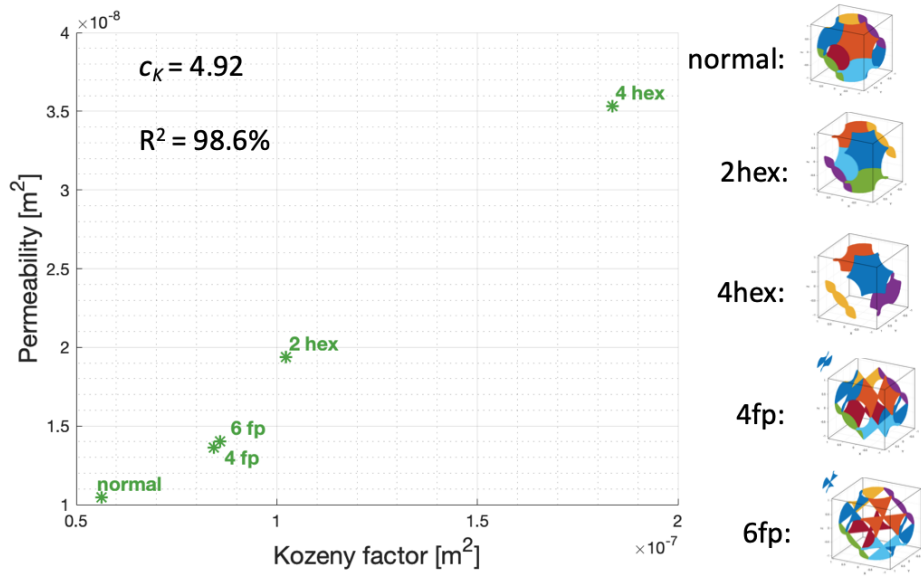


Figure 4.10: Relation between permeability and Kozeny factor for Schwarz P samples.

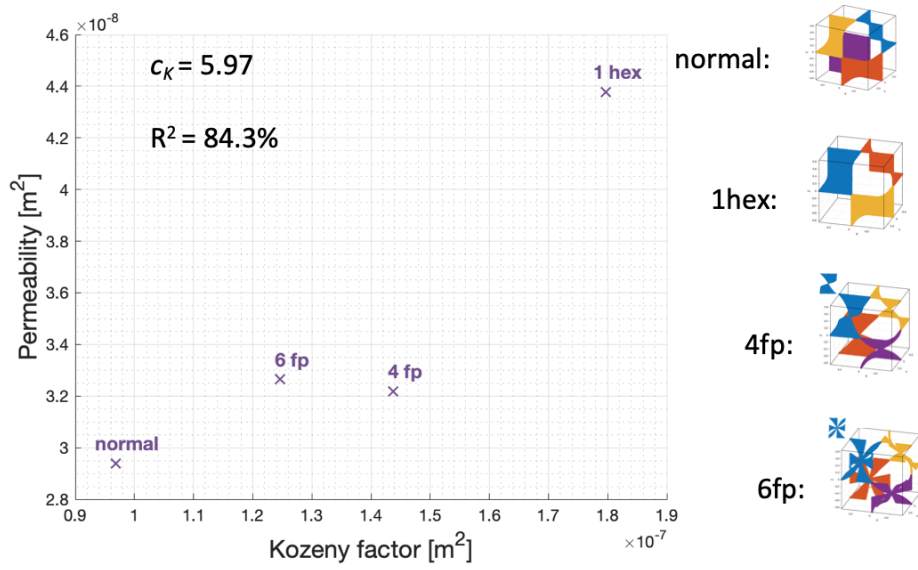


Figure 4.11: Relation between permeability and Kozeny factor for Schwarz D samples.

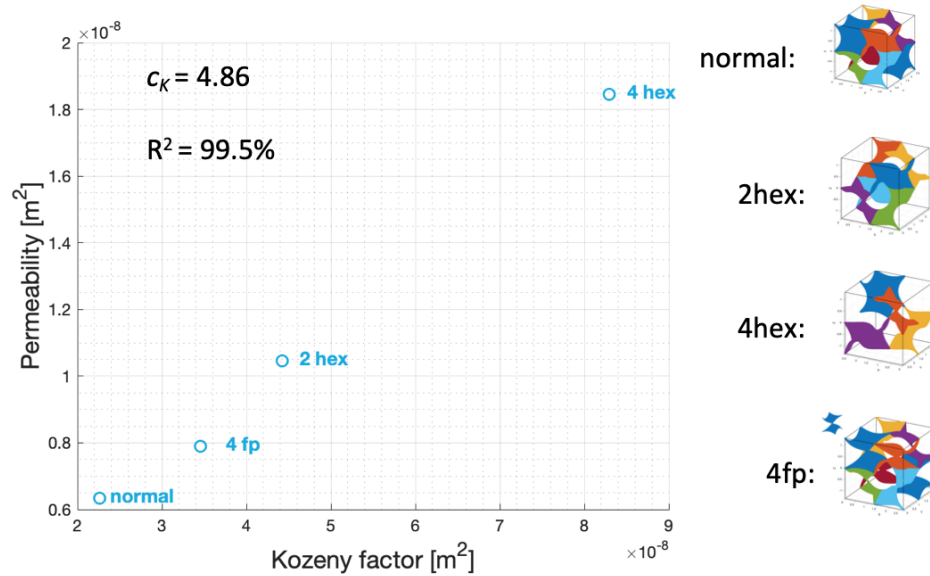


Figure 4.12: Relation between permeability and Kozeny factor for Gyroid samples.

In the figures above the agreement between the theory and simulation results is evident for the P and G families. Permeability is linearly proportional to the Kozeny factor, which combines porosity and specific surface area of the samples. Nevertheless, in the D group, the relation between *4 fund. patches* and *6 fund. patches* designs is disturbed according to the Kozeny theory.

Unfortunately, it was not feasible to estimate Kozeny factor for the printed samples, due to the complexity of acquiring the surface area values for the porous scaffolds.

5

Discussion

The central research problem of this thesis was to evaluate the effect of extra channels inclusion in Schwarz P, Schwarz D and Gyroid scaffolds on the mass transfer and mechanical properties.

5.1. Experiment results

The obtained results indicate that by excision of fundamental patches from the original surface permeability can be increased up to 240% compared to the unmodified scaffolds (*P without 4 hexagons*, *G without 4 hexagons*), while Young's modulus and yield stress decrease with the material removal. For instance, the stiffness of the previously mentioned designs was less than 30% of the primary value. Roughly 50% material excision explains an extreme reduction in stiffness and yield strength for these two designs, whereas the other designs showed to be more balanced on these two aspects. They showed a more reasonable trade-off between permeability improvement and stiffness decrease. The most efficient designs were found in the Gyroid family group, and more precisely the design *without 2 hexagons* (permeability increased by 40% and stiffness constituting 60% of the unmodified scaffold). Results of the designs *with 4 and 6 fundamental patches removed* from Schwarz P unit cell were close to each other with 40% permeability raise and 50% stiffness reduction. There was no middle ground design in the D surface group due to the brittle nature of the scaffolds. It can be explained by hexagons horizontal and vertical orientation in relation to the applied load, which causes local stress concentration and fracture consequently. In the Schwarz P and Gyroid designs, the smoothly curved walls enabled gradual compression of layers. The most efficient one in the D group can be considered the random design with 120% permeability and 50% elastic gradient ratios.

The other designs should not be underestimated since they suggest other possibilities of the material performance. The common problem with the widely applied biomaterial Ti-6Al-4V is high stiffness of the bone tissue implants produced from this alloy. In the study of Bobbert *et al.* the Ti-6Al-4V TPMS scaffolds had stiffness in the range 3.2 — 6.4 *GPa*, while the stiffness of trabecular bone tissue is of the order of hundreds *MPa* (value heavily depends on location in the human body) [10]. For the same samples, the permeability and porosity were in the range of trabecular bone [10]. With the described here design approach the problem of stress shielding can be solved, without compromising the permeability and

porosity parameters.

Since my samples were fabricated from non-biocompatible material, plastic, the absolute values of the mechanical parameters, stiffness and yield stress, can not be directly used to judge about the applicability of the designed structures in orthopaedic implants. However, one can look at the ratio of scaffolds stiffness to bulk material stiffness. Young's modulus of the post-cured Grey Pro resin is 2.6 GPa , which means that classic Schwarz P architecture with 69% porosity accounts for 1.5% of the original stiffness, Gyroid 55% porosity — 2.3%, Schwarz D, 78% porosity, — also 1.5%. Despite the surprisingly significant mechanical performance deterioration, the numbers for the non-modified samples are in a good agreement with the other studies related to the investigation of TPMS scaffolds with similar porosity range [10, 35, 37]. The material applicability problem does not concern the permeability values since it mostly depends on the arrangement of the material and not its characteristics. The reported permeability of trabecular bone varies between $0.4 - 15 \times 10^{-9} \text{ m}^2$, which incorporates the range of measured permeability values of the samples $0.72 - 3.46 \times 10^{-9} \text{ m}^2$ [24, 39].

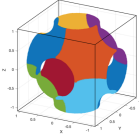
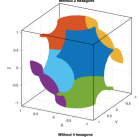
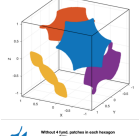
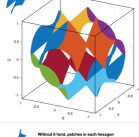
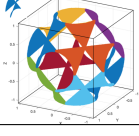
5.2. Fabrication issues

In the section 3.2.4, regarding the outcome of the micro-CT scan, the mismatch between the designed scaffolds and printed ones is clear. The thickness of the walls was extremely higher than the aimed $200 \mu\text{m}$, with the mean thickness values ranging between $282 \mu\text{m}$ and $322 \mu\text{m}$. The samples were printed in three sets, each with one specific TPMS designs. So, all the samples inspired by Schwarz P geometry were printed together. Thus it could have been expected that thickness values would be similar at least for the samples printed together. However, this was not the case, according to the table 3.4. This could be probably explained by the position of the samples on the platform and printing on the edge of the printer resolution. Also, the dimensions of the samples did not agree with the assigned $10 \text{ mm} \times 10 \text{ mm} \times 16 \text{ mm}$. The mean height of the 80 samples was 15.75 mm with standard deviation of 0.40 mm , the average cross-section area was 97.33 mm^2 with standard deviation of 3.92 mm^2 . It was also noticed that the unit cell size was gradually changing from bottom to top layers, with bottom layers being more shrunken. The variation was minor but still visible to the unaided eye. In this case, the temperature regime can be the major reason. In the SLA printer, the samples are produced upside down, starting from the bottom layers. The starting print temperature is around 31°C and continues heating to the target printing temperature around 35°C . Also, the bottom layers spend more time in the printer cavity atop of the heated resin. For the samples with larger feature size, this fact can be ignored, but for my samples it apparently played a significant role.

5.3. Quantitative model results

In the following table, the permeability values measured experimentally are presented next to the model prediction.

Table 5.1: Comparison between experimental (exp.) and simulation (sim.) permeability values for the regular designs for Schwarz P design group. For the experimental data the values are given in the format *mean (SD)*.

Design	Unit cell	Porosity	Permeability	Porosity	Permeability
		(exp.) %	(exp.) $10^{-9} m^2$	(sim.) %	(sim.) $10^{-9} m^2$
P normal		68.5 (0.9)	1.527 (0.092)	74.8	10.468
2 hexagons		77.3 (1.2)	1.816 (0.054)	80.2	19.390
4 hexagons		84.0 (0.8)	3.463 (0.310)	85.2	35.312
4 fund. patches		72.7 (1.1)	2.200 (0.041)	79.7	13.645
6 fund. patches		77.7 (0.4)	2.173 (0.051)	81.2	14.004

To better visualise the relation of permeability values of different designs to each other the following graph is created:

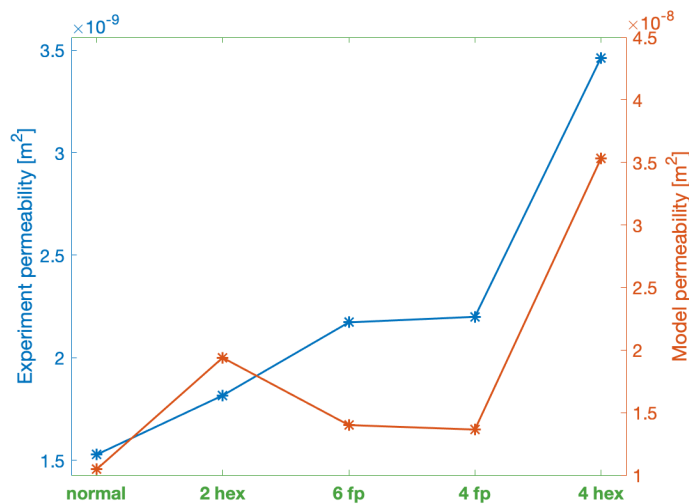
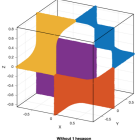
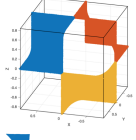
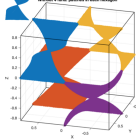
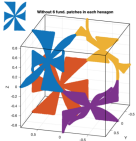


Figure 5.1: Permeability trend in the experiment and the model for Schwarz P design group. The blue line corresponds to the experimental results, while the orange one — to the simulation. The Y axis have different scale.

Table 5.2: Comparison between experimental (exp.) and simulation (sim.) permeability values for the regular designs for Schwarz D design group.

Design	Unit cell	Porosity	Permeability	Porosity	Permeability
		(exp.) %	(exp.) $10^{-9} m^2$	(sim.) %	(sim.) $10^{-9} m^2$
D normal		78.2 (0.6)	2.154 (0.044)	79.5	29.378
1 hexagon		83.8 (0.7)	2.546 (0.088)	84.1	43.767
4 fund. patches		82.0 (0.6)	2.061 (0.040)	83.8	32.174
6 fund. patches		81.8 (0.9)	2.204 (0.047)	83.8	32.641

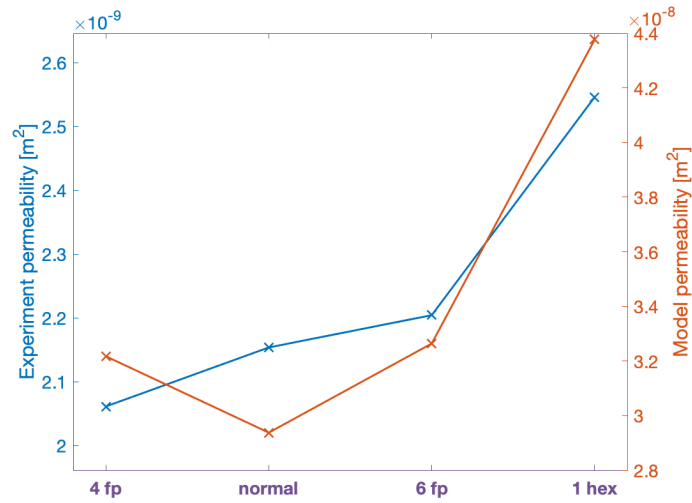
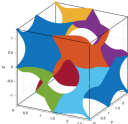
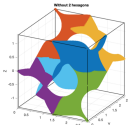
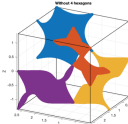
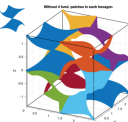


Figure 5.2: Permeability trend in the experiment and the model for Schwarz D design group.

Table 5.3: Comparison between experimental (exp.) and simulation (sim.) permeability values for the regular designs for Gyroid design group.

Design	Unit cell	Porosity	Permeability	Porosity	Permeability
		(exp.) %	(exp.) $10^{-9} m^2$	(sim.) %	(sim.) $10^{-9} m^2$
G normal		55.4 (0.9)	0.716 (0.080)	66.7	6.333
2 hexagons		67.1 (0.6)	1.007 (0.054)	73.7	10.453
4 hexagons		76.9 (0.7)	1.678 (0.028)	79.9	18.445
4 fund. patches		70.2 (1.5)	1.185 (0.062)	72.9	7.895

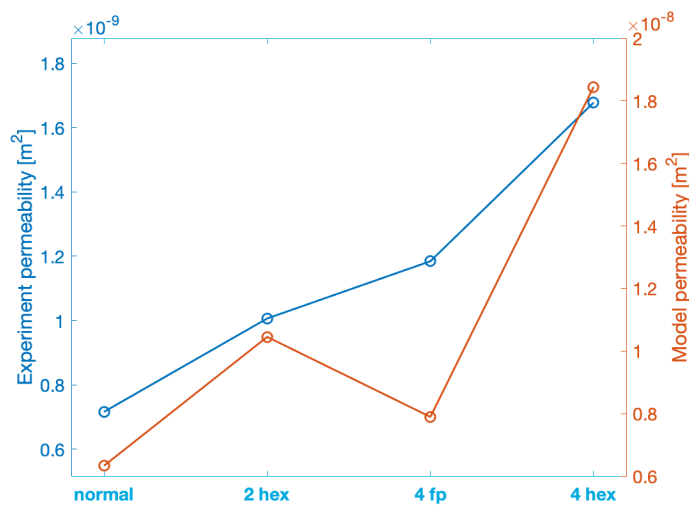


Figure 5.3: Permeability trend in the experiment and the model for Gyroid design group

Values predicted by the model are prominently higher than the measured ones. This was already expected from the lower porosity values of the real samples compared to the designed ones and the micro-CT scan results. Moreover, the agreement in the trend between the experiment and simulation was not preserved for any of the design groups, which was visualised in the figures 5.1, 5.2, 5.3. For the Gyroid scaffolds the order was violated for the designs *without 2 hexagons* and *without 4 fund. patches*. According to the model, the latter was less permeable. But according to the experiment, it has higher permeability coefficient. The same appeared in the Schwarz P group for the designs *without 2 hexagons*,

without 4 fund. patches and *without 6 fund. patches*. In the Schwarz D group, the experiment results shown the non-modified surface to be more permeable than the one with removed material, *without 4 fund. patches*. The model predictions were opposite for these two designs. The exact reason behind this problem is hard to assess. The main suspicion fell on the quality of the 3D printed samples. To prove my hypothesis, the samples with double unit cell size were fabricated and subjected to the permeability test. It was assumed that samples with a larger feature size would match the design better.

Unfortunately, it was not feasible to print and test another 80 samples. That is why I selected two designs with the inverted trend: *Schwarz P without 2 hexagons* and *Schwarz P without 4 fund. patches*. Ten samples with 4 mm unit cell size and 400 μm wall thickness were fabricated, two samples failed during the printing.

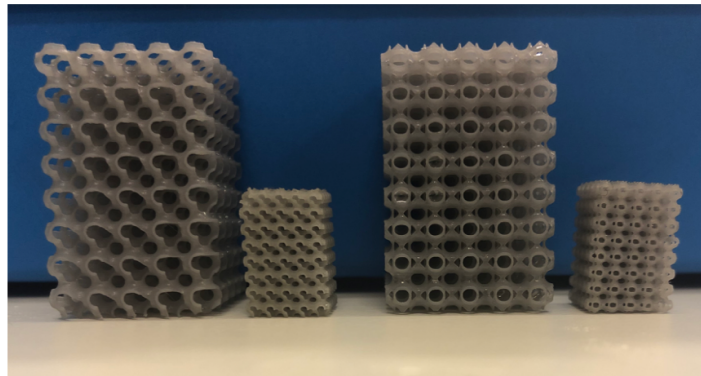


Figure 5.4: New samples next to the old ones. From left to right: *without 2 hexagons*, *without 4 fund. patches*.

The dimensions of the new scaffolds allied decently with the assigned $20\text{ mm} \times 20\text{ mm} \times 32\text{ mm}$. The mean height of the 8 samples was 31.37 mm with standard deviation of 0.25 mm , the average cross-section area was 399.1 mm^2 with standard deviation of 1.95 mm^2 . Because of the enlarged pore sizes, the water flow through the scaffolds could not be considered laminar anymore. To solve this problem, the more viscous solution of water and glycerol was prepared. The density and dynamic viscosity of the solution at 20°C were 1129.6 kg/m^3 and $6.2e-3\text{ Pa}\cdot\text{s}$. Extracted porosity and permeability values from the falling head test are presented in the table 5.4.

Table 5.4: The experimental results of the new samples.

Design	Porosity	Permeability
	%	10^{-9} m^2
P 2 hexagons	82.7 (0.2)	20.420 (0.620)
P 4 fund. patches	81.2 (0.4)	24.525 (1.638)

The experiment refuted the hypothesis and proved the accuracy of the previous result.

Another evident difference between the experiment and the model is that in the model only a quarter of one layer is simulated. Apparently, it was not sufficient to predict accurate

results. However, the coarse mesh of the quarter already comprised of approximately 25 000 faces and was already close to the limit of SolidWorks performance. The model also did not encounter the samples' material properties like roughness and wettability. These parameters were proved to significantly affect the flow through the porous media [5, 43]. Also, the non-uniform wall thickness in the samples, proven by the CT scan, could not be embedded in the model.

All these factors push the real experiment and the model away from each other, resulting in the discrepancy of the permeability values.

5.4. Qualitative model results

The computational model provides velocity and wall shear stress distribution fields, which are hard to access experimentally in the porous media. Doppler optical coherence tomography or nuclear magnetic resonance velocimetry technique are commonly used for visualisation of interstitial flow within porous materials [28, 36]. In our group, these experiments could not be performed.

From the fluid dynamics simulations, the average wall shear stress lies in between 57 mPa and 145 mPa . I consider, these values to be relevant also for the printed samples because the stresses are proportional to the velocity gradient and not to its absolute value. The reported physiological range in the bone matrix is limited by 10 mPa , due to the extremely slow flow of extravascular fluid [33]. However, *in vitro* studies, gathered in the review of Wittkowske *et al.*, showed that osteocytes and osteoblasts respond to a wide range of wall shear stresses, up to 2 Pa [55]. It was also shown that better organised bone apatite crystals were formed under fluid shear stress below 1 Pa [41]. These facts add arguments in favour of TPMS structures in general and developed designs in particular.

6

Conclusions and outlook

In my master thesis project, I aimed to investigate how fundamental patches removal from the original TPMS structures would affect its permeability, porosity and mechanical properties. Based on experimental and computational results, it can be concluded that the developed design approach has a strong potential in the improvement of mass transfer and compliance properties compared to the non-modified TPMS structures. The measured characteristic parameters of the created metamaterial are shown to be in a good agreement with the previously reported values. Moreover, the range of permeability and porosity values for trabecular bone encompasses the corresponding parameters of the fabricated scaffolds. The absolute values of the stiffness and the yield stress of the designed scaffold can not be directly utilised to evaluate the applicability of the material in the orthopaedic implants. But the percentagewise ratios to the bulk material properties suggest a reasonable decline in elastic gradient and yield strength.

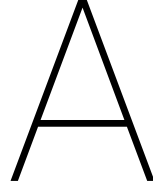
The novelty of this research is also in the extensive implementation of the mathematical background of Triply Periodic Minimal Surfaces. The established design approach relies on the Weierstrass equations and presence of the smallest building block in the TPMS unit cells, fundamental patch. Despite the huge number of possible designs, which can be created with my method, the presented ones are considered to be the most relevant in practical terms: the introduced pore size exceeded the $300\ \mu m$, the connectivity of the structures was not impaired and the porosity of the scaffolds remained in the trabecular bone range. Moreover, the random method, incorporating the graph theory, provides an extra opportunity to imitate the randomness of the bone structure.

The developed COMSOL model gave insight into the flow velocity distribution through the samples and induced wall shear stresses. The latter is directly linked to regenerative properties of the porous material, influencing bone metabolism. According to the simulation results, the developed scaffolds induce mechanical stimulation in the physiological range. The difference in the average flow-induced wall shear stress and total shear force between the scaffolds also suggests that biomechanical properties of the material can be tailored with the presented here design method. However, the future model adjustments are necessary for the reliable predictions of the material permeability coefficients.

Further, alternative biocompatible materials, like Ti-6Al-4V alloy, can be used to print scaffolds to discover the effect of different bulk material properties on the presented designs. Also, the developed approach is not limited by the three selected TPMS. For instance, I-WP minimal surface could be employed, for which Weierstrass representation was found only recently [14]. Another interesting idea to develop this research further is to design a material with a gradual change of the material removed. This way the bone structure with cortical and trabecular parts can be imitated.

Overall, I hope that the original idea of this thesis will be developed further, and the metamaterials will be applied in the biomechanical research fields.

Appendices



Combined experimental results

Table A.1: Combined table of the experiment results. The values are given in the format *mean (SD)*.

	Design	Porosity	Permeability	Elastic gradient	Yield stress	Plateau stress
		%	$10^{-9} m^2$	<i>MPa</i>	<i>MPa</i>	<i>MPa</i>
P	normal	68.5 (0.9)	1.527 (0.092)	35.241 (4.319)	2.261 (0.193)	2.585 (0.095)
	2 hexagons	77.3 (1.2)	1.816 (0.054)	12.867 (2.862)	0.854 (0.187)	0.940 (0.146)
	4 hexagons	84.0 (0.8)	3.463 (0.310)	10.796 (2.924)	0.485 (0.067)	0.886 (0.051)
	4 fund. patch.	72.7 (1.1)	2.200 (0.041)	17.379 (4.761)	1.048 (0.262)	1.418 (0.193)
	6 fund. patch.	77.7 (0.4)	2.173 (0.051)	17.312 (2.178)	0.968 (0.140)	1.218 (0.118)
	random	76.8 (0.8)	1.992 (0.061)	14.070 (2.130)	0.726 (0.118)	1.217 (0.122)
D	normal	78.2 (0.6)	2.154 (0.044)	36.309 (7.734)	2.265 (0.371)	2.796 (0.280)
	1 hexagon	83.8 (0.7)	2.546 (0.088)	6.598 (1.261)	0.189 (0.065)	0.922 (0.126)
	4 fund. patch.	82.0 (0.6)	2.061 (0.040)	22.190 (2.837)	1.115 (0.259)	1.205 (0.061)
	6 fund. patch.	81.8 (0.9)	2.204 (0.047)	24.194 (5.937)	1.573 (0.415)	1.658 (0.209)
	random	83.8 (0.6)	2.593 (0.051)	17.210 (1.173)	0.790 (0.129)	1.102 (0.130)
G	normal	55.4 (0.9)	0.716 (0.080)	54.969 (2.984)	3.076 (0.057)	4.225 (0.090)
	2 hexagons	67.1 (0.6)	1.007 (0.054)	33.611 (3.956)	1.928 (0.181)	2.359 (0.221)
	4 hexagons	76.9 (0.7)	1.678 (0.028)	13.148 (2.107)	0.734 (0.081)	0.953 (0.111)
	4 fund. patch.	70.2 (1.5)	1.185 (0.062)	13.057 (1.266)	0.940 (0.194)	1.287 (0.146)
	random	69.1 (1.7)	1.351 (0.055)	21.751 (3.797)	1.236 (0.159)	1.804 (0.229)

B

Results of the t-test

Table B.1: P-values from the t-test applied to the permeability data of the P samples. * - hexagon; ** - fundamental patch.

	normal	2 hex*	4 hex	4 fp**	6 fp	random
normal		0.036	<0.001	<0.001	<0.001	<0.001
2 hex			<0.001	<0.001	0.0012	0.014
4 hex				<0.001	<0.001	<0.001
4 fp					<u>0.2748</u>	0.0065
6 fund. p						0.0121
random						

Table B.2: P-values from the t-test applied to the permeability data of the D samples. The p-values more than significance level are underlined.

	normal	1 hex	4 fp	6 fp	random
normal		0.0024	0.0093	<u>0.1727</u>	<0.001
1 hex			<0.001	0.0015	<u>0.3215</u>
4 fp				0.0111	<0.001
6 fp					<0.001
random					

Table B.3: P-values from the t-test applied to the permeability data of the G samples.

	normal	2 hex	4 hex	4 fp	random
normal		0.0061	<0.001	<0.001	<0.001
2 hex			<0.001	0.0146	<0.001
4 hex				<0.001	<0.001
4 fp					0.0291
random					

Table B.4: P-values from the t-test applied to the elastic gradient data of the P samples.

	normal	2 hex	4 hex	4 fp	6 fp	random
normal		<0.001	<0.001	<0.001	<0.001	<0.001
2 hex			<u>0.2361</u>	<u>0.0703</u>	0.0255	<u>0.5726</u>
4 hex				0.0389	0.0133	<u>0.0887</u>
4 fp					<u>0.9759</u>	<u>0.1938</u>
6 fp						0.0445
random						

Table B.5: P-values from the t-test applied to the elastic gradient data of the D samples. The p-values more than significance level are underlined.

	normal	1 hex	4 fp	6 fp	random
normal		0.0016	0.0122	<u>0.0667</u>	0.0042
1 hex			<0.001	0.0015	<0.001
4 fp				<u>0.3399</u>	0.0066
6 fp					0.0448
random					

Table B.6: P-values from the t-test applied to the elastic gradient data of the G samples.

	normal	2 hex	4 hex	4 fp	random
normal		<0.001	<0.001	<0.001	<0.001
2 hex			<0.001	<0.001	0.0032
4 hex				<u>0.9411</u>	0.0014
4 fp					0.0134
random					

Table B.7: P-values from the t-test applied to the yield stress data of the P samples.

	normal	2 hex	4 hex	4 fp	6 fp	random
normal		<0.001	<0.001	0.010	<0.001	<0.001
2 hex			0.0156	<u>0.0934</u>	<u>0.2095</u>	<u>0.3449</u>
4 hex				0.0071	<0.001	0.0217
4 fp					<u>0.5583</u>	<u>0.0804</u>
6 fp						<u>0.0858</u>
random						

Table B.8: P-values from the t-test applied to the yield stress data of the D samples. The p-values more than significance level are underlined.

	normal	1 hex	4 fp	6 fp	random
normal		<0.001	0.0014	<u>0.0740</u>	0.0020
1 hex			0.0014	0.0016	<0.001
4 fp				<u>0.1915</u>	<u>0.1120</u>
6 fp					0.0049
random					

Table B.9: P-values from the t-test applied to the yield stress data of the G samples.

	normal	2 hex	4 hex	4 fp	random
normal		<0.001	<0.001	<0.001	<0.001
2 hex			<0.001	0.0023	<0.001
4 hex				<u>0.1271</u>	<0.001
4 fp					<u>0.1167</u>
random					

Table B.10: P-values from the t-test applied to the plateau stress data of the P samples.

	normal	2 hex	4 hex	4 fp	6 fp	random
normal		<0.001	<0.001	<0.001	<0.001	<0.001
2 hex			<u>0.3089</u>	<0.001	0.0213	<u>0.0506</u>
4 hex				0.0021	0.0029	0.0058
4 fp					<u>0.0882</u>	<u>0.1705</u>
6 fp						<u>0.9888</u>
random						

Table B.11: P-values from the t-test applied to the plateau stress data of the D samples. The p-values more than significance level are underlined.

	normal	1 hex	4 fp	6 fp	random
normal		<0.001	<0.001	0.032	<0.001
1 hex			0.0078	0.0058	<u>0.1510</u>
4 fp				0.0096	<u>0.1331</u>
6 fp					0.0040
random					

Table B.12: P-values from the t-test applied to the plateau stress data of the G samples.

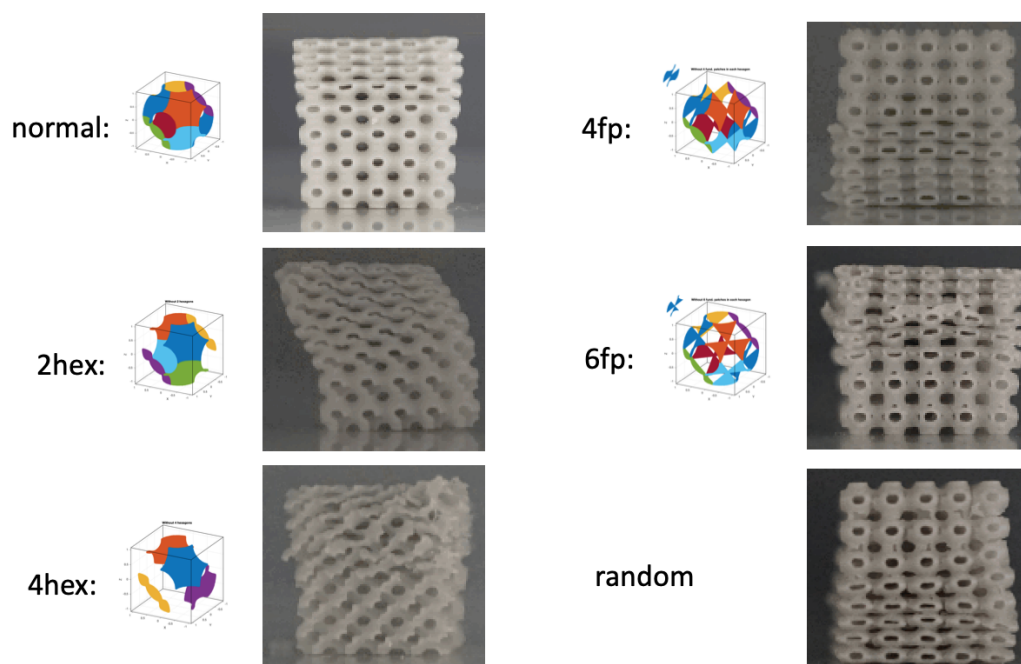
	normal	2 hex	4 hex	4 fp	random
normal		<0.001	<0.001	<0.001	<0.001
2 hex			<0.001	0.0015	0.0020
4 hex				0.0359	<0.001
4 fp					0.0257
random					

C

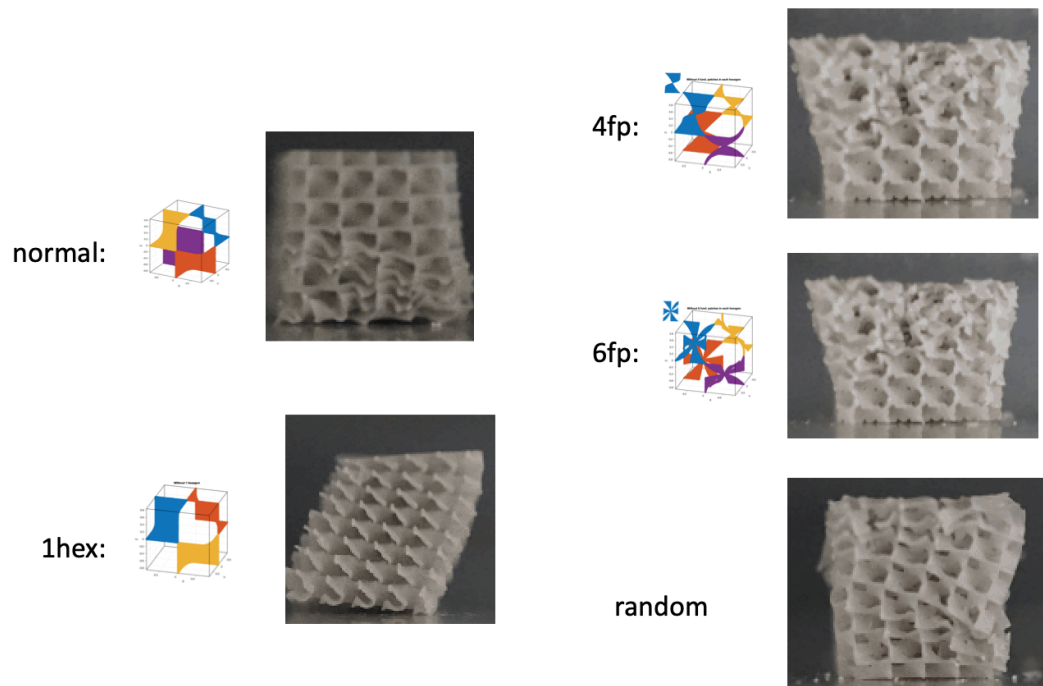
Failure modes of the samples

The scaffolds after the compression test with the corresponding unit cell geometry:

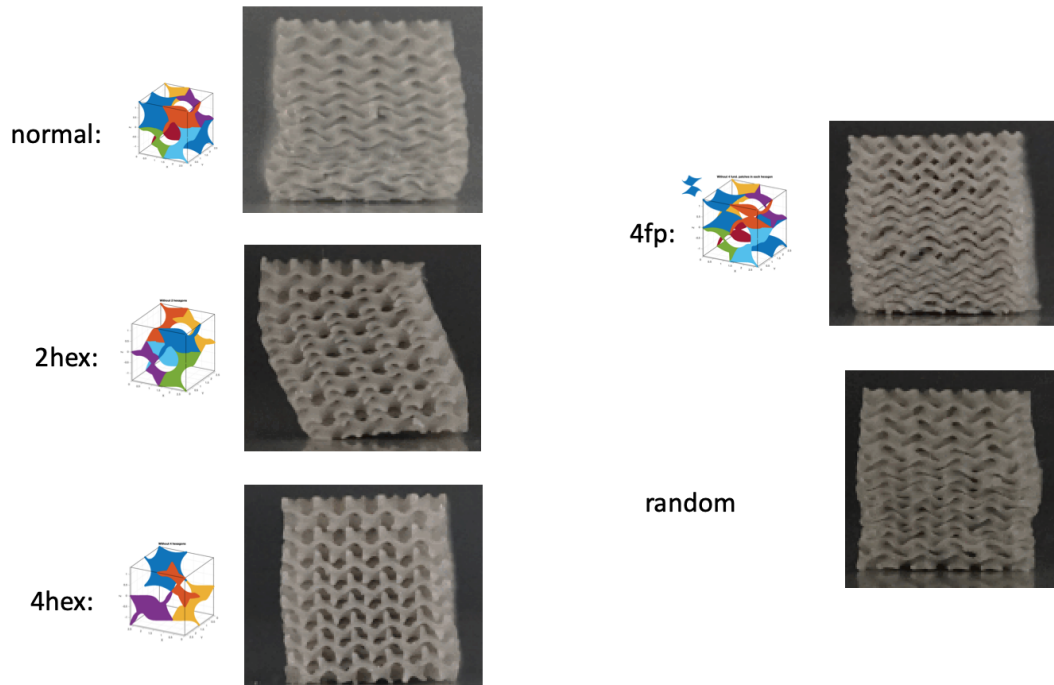
Schwarz P



Schwarz D



Gyroid



Bibliography

- [1] Preform software: Prepare your models for printing. URL <https://formlabs.com/software/#preform>.
- [2] Mechanical properties of materials. URL <https://mechanicalc.com/reference/mechanical-properties-of-materials>.
- [3] Compare formlabs sla 3d printer tech specs, 2019. URL <https://formlabs.com/3d-printers/form-3/tech-specs/>.
- [4] Functional prototyping materials for engineers, 2019. URL <https://formlabs.com/materials/engineering/#grey-pro-resin>.
- [5] William G Anderson et al. Wettability literature survey part 5: the effects of wettability on relative permeability. *Journal of Petroleum Technology*, 39(11):1–453, 1987.
- [6] Fausto Bernardini, Joshua Mittleman, Holly Rushmeier, Cláudio Silva, and Gabriel Taubin. The ball-pivoting algorithm for surface reconstruction. *IEEE transactions on visualization and computer graphics*, 5(4):349–359, 1999.
- [7] Cécile M Bidan, Krishna P Kommareddy, Monika Rumpfer, Philip Kollmannsberger, Yves JM Bréchet, Peter Fratzl, and John WC Dunlop. How linear tension converts to curvature: geometric control of bone tissue growth. *PloS one*, 7(5):e36336, 2012.
- [8] Cécile M Bidan, Krishna P Kommareddy, Monika Rumpfer, Philip Kollmannsberger, Peter Fratzl, and John WC Dunlop. Geometry as a factor for tissue growth: towards shape optimization of tissue engineering scaffolds. *Advanced healthcare materials*, 2(1):186–194, 2013.
- [9] Sébastien BG Blanquer, Maïke Werner, Markus Hannula, Shahriar Sharifi, Guillaume PR Lajoie, David Eglin, Jari Hyttinen, André A Poot, and Dirk W Grijpma. Surface curvature in triply-periodic minimal surface architectures as a distinct design parameter in preparing advanced tissue engineering scaffolds. *Biofabrication*, 9(2):025001, 2017.
- [10] FSL Bobbert, K Lietaert, Ali Akbar Eftekhari, B Pouran, SM Ahmadi, H Weinans, and AA Zadpoor. Additively manufactured metallic porous biomaterials based on minimal surfaces: A unique combination of topological, mechanical, and mass transport properties. *Acta biomaterialia*, 53:572–584, 2017.
- [11] Ossian Bonnet. Sur une propriété de maximum relative à la sphère. *Nouvelles annales de mathématiques: journal des candidats aux écoles polytechnique et normale*, 12:433–438, 1853.

- [12] Paolo Cignoni, Marco Callieri, Massimiliano Corsini, Matteo Dellepiane, Fabio Ganovelli, and Guido Ranzuglia. MeshLab: an Open-Source Mesh Processing Tool. In Vittorio Scarano, Rosario De Chiara, and Ugo Erra, editors, *Eurographics Italian Chapter Conference*. The Eurographics Association, 2008. ISBN 978-3-905673-68-5. doi: 10.2312/LocalChapterEvents/ItalChap/ItalianChapConf2008/129-136.
- [13] Wikimedia Commons. File:hausdorff distance sample.svg — wikimedia commons, the free media repository, 2019. URL https://commons.wikimedia.org/w/index.php?title=File:Hausdorff_distance_sample.svg&oldid=333436981. [Online; accessed 13-September-2019].
- [14] Djurdje Cvijović and Jacek Klinowski. The computation of the triply periodic i-wp minimal surface. *Chemical physics letters*, 226(1-2):93–99, 1994.
- [15] Yadolah Dodge. *The concise encyclopedia of statistics*. Springer Science & Business Media, 2008.
- [16] Michael Doube, Michał M Kłosowski, Ignacio Arganda-Carreras, Fabrice P Cordelières, Robert P Dougherty, Jonathan S Jackson, Benjamin Schmid, John R Hutchinson, and Sandra J Shefelbine. Bonej: free and extensible bone image analysis in imagej. *Bone*, 47(6):1076–1079, 2010.
- [17] W Fischer. Spanning minimal surfaces. *Phil. Trans. R. Soc. Lond. A*, 354(1715):2105–2142, 1996.
- [18] Andrew Fogden and Stephan T Hyde. Continuous transformations of cubic minimal surfaces. *The European Physical Journal B-Condensed Matter and Complex Systems*, 7(1):91–104, 1999.
- [19] Paul JF Gandy and Jacek Klinowski. Exact computation of the triply periodic g (gyroid') minimal surface. *Chemical Physics Letters*, 321(5-6):363–371, 2000.
- [20] Paul JF Gandy and Jacek Klinowski. Exact computation of the triply periodic schwarz p minimal surface. *Chemical Physics Letters*, 322(6):579–586, 2000.
- [21] Paul JF Gandy, Djurdje Cvijović, Alan L Mackay, and Jacek Klinowski. Exact computation of the triply periodic d (diamond') minimal surface. *Chemical physics letters*, 314(5-6):543–551, 1999.
- [22] Z Gorgin Karaji, Mathew Speirs, Sasan Dadbakhsh, J-P Kruth, HIED Weinans, AA Zadpoor, and SIED Amin Yavari. Additively manufactured and surface biofunctionalized porous nitinol. *ACS applied materials & interfaces*, 9(2):1293–1304, 2017.
- [23] RA Greenkorn. Steady flow through porous media. *AIChE Journal*, 27(4):529–545, 1981.
- [24] Michèle J Grimm and John L Williams. Measurements of permeability in human calcaneal trabecular bone. *Journal of Biomechanics*, 30(7):743–745, 1997.
- [25] Xue-Nan Gu and Yu-Feng Zheng. A review on magnesium alloys as biodegradable materials. *Frontiers of Materials Science in China*, 4(2):111–115, 2010.

- [26] Stephen Hyde, Z Blum, T Landh, S Lidin, BW Ninham, S Andersson, and K Larsson. *The language of shape: the role of curvature in condensed matter: physics, chemistry and biology*. Elsevier, 1996.
- [27] ISO13314 ISO. Mechanical testing of metals—ductility testing—compression test for porous and cellular metals, 2011. 2011.
- [28] Yali Jia, Pierre-Olivier Bagnaninchi, Ying Yang, Alicia J El Haj, Monica T Hinds, Sean J Kirkpatrick, and Ruikang Wang. Doppler optical coherence tomography imaging of local fluid flow and shear stress within microporous scaffolds. *Journal of biomedical optics*, 14(3):034014, 2009.
- [29] J Kadkhodapour, H Montazerian, A Ch Darabi, A Zargarian, and S Schmauder. The relationships between deformation mechanisms and mechanical properties of additively manufactured porous biomaterials. *Journal of the mechanical behavior of biomedical materials*, 70:28–42, 2017.
- [30] Sebastian C Kapfer, Stephen T Hyde, Klaus Mecke, Christoph H Arns, and Gerd E Schröder-Turk. Minimal surface scaffold designs for tissue engineering. *Biomaterials*, 32(29):6875–6882, 2011.
- [31] FS Kaplan, WC Hayes, TM Keaveny, A Boskey, TA Einhorn, and JP Iannotti. Form and function of bone. *Orthopaedic basic science*, pages 127–185, 1994.
- [32] Vassilis Karageorgiou and David Kaplan. Porosity of 3d biomaterial scaffolds and osteogenesis. *Biomaterials*, 26(27):5474–5491, 2005.
- [33] Kyung Min Kim, Yoon Jung Choi, Jun-Ha Hwang, A Rum Kim, Hang Jun Cho, Eun Sook Hwang, Joong Yull Park, Sang-Hoon Lee, and Jeong-Ho Hong. Shear stress induced by an interstitial level of slow flow increases the osteogenic differentiation of mesenchymal stem cells through taz activation. *PloS one*, 9(3):e92427, 2014.
- [34] J Knychala, N Bouropoulos, CJ Catt, OL Katsamenis, CP Please, and BG Sengers. Pore geometry regulates early stage human bone marrow cell tissue formation and organisation. *Annals of biomedical engineering*, 41(5):917–930, 2013.
- [35] Lan Li, Jianping Shi, Kaijia Zhang, Longfei Yang, Fei Yu, Liya Zhu, Huixin Liang, Xingsong Wang, and Qing Jiang. Early osteointegration evaluation of porous ti6al4v scaffolds designed based on triply periodic minimal surface models. *Journal of Orthopaedic Translation*, 2019.
- [36] Julia J Mack, Khalid Youssef, Onika DV Noel, Michael P Lake, Ashley Wu, M Luisa Iruela-Arispe, and Louis-S Bouchard. Real-time maps of fluid flow fields in porous biomaterials. *Biomaterials*, 34(8):1980–1986, 2013.
- [37] H Montazerian, E Davoodi, M Asadi-Eydivand, J Kadkhodapour, and M Solati-Hashjin. Porous scaffold internal architecture design based on minimal surfaces: A compromise between permeability and elastic properties. *Materials & Design*, 126: 98–114, 2017.
- [38] COMSOL Multiphysics. Comsol. Inc., Burlington, MA, www.comsol.com.

- [39] Eric A Nauman, KE Fong, and TM Keaveny. Dependence of intertrabecular permeability on flow direction and anatomic site. *Annals of Biomedical Engineering*, 27(4): 517–524, 1999.
- [40] Naoki Nishiyama and Tadashi Yokoyama. Permeability of porous media: Role of the critical pore size. *Journal of Geophysical Research: Solid Earth*, 122(9):6955–6971, 2017.
- [41] Xufeng Niu, Liyang Wang, Feng Tian, Lizhen Wang, Ping Li, Qingling Feng, and Yubo Fan. Shear-mediated crystallization from amorphous calcium phosphate to bone apatite. *Journal of the mechanical behavior of biomedical materials*, 54:131–140, 2016.
- [42] Andy L Olivares, Èlia Marsal, Josep A Planell, and Damien Lacroix. Finite element study of scaffold architecture design and culture conditions for tissue engineering. *Biomaterials*, 30(30):6142–6149, 2009.
- [43] Sylvain Pasquier, Michel Quintard, and Yohan Davit. Modeling flow in porous media with rough surfaces: Effective slip boundary conditions and application to structured packings. *Chemical Engineering Science*, 165:131–146, 2017.
- [44] F Pennella, G Cerino, D Massai, D Gallo, G Falvo D’Urso Labate, Alessandro Schiavi, MA Deriu, A Audenino, and Umberto Morbiducci. A survey of methods for the evaluation of tissue engineering scaffold permeability. *Annals of biomedical engineering*, 41(10):2027–2041, 2013.
- [45] Monika Rumpler, Alexander Woesz, John WC Dunlop, Joost T van Dongen, and Peter Fratzl. The effect of geometry on three-dimensional tissue growth. *Journal of the Royal Society Interface*, 5(27):1173–1180, 2008.
- [46] D Schaefer, I Martin, P Shastri, RF Padera, R Langer, LE Freed, and G Vunjak-Novakovic. In vitro generation of osteochondral composites. *Biomaterials*, 21(24): 2599–2606, 2000.
- [47] Johannes Schindelin, Ignacio Arganda-Carreras, Erwin Frise, Verena Kaynig, Mark Longair, Tobias Pietzsch, Stephan Preibisch, Curtis Rueden, Stephan Saalfeld, Benjamin Schmid, et al. Fiji: an open-source platform for biological-image analysis. *Nature methods*, 9(7):676, 2012.
- [48] Alan Hugh Schoen. Infinite periodic minimal surfaces without self-intersections. 1970.
- [49] Hermann Amandus Schwarz. Bestimmung einer speciellen minimalfläche. In *Gesammelte Mathematische Abhandlungen*, pages 6–91. Springer, 1890.
- [50] Anatoliy Sheypak. *Ch. 1: Basics of gas and fluid mechanics*. MSIU, 2007.
- [51] Nurshaun Sreedhar, Navya Thomas, Oraib Al-Ketan, Reza Rowshan, Hector H Hernandez, Rashid K Abu Al-Rub, and Hassan A Arafat. Mass transfer analysis of ultrafiltration using spacers based on triply periodic minimal surfaces: Effects of spacer design, directionality and voidage. *Journal of Membrane Science*, 561:89–98, 2018.

- [52] I Standard. Iso 13314: 2011 (e)(2011) mechanical testing of metals—ductility testing—compression test for porous and cellular metals. *Ref number ISO*, 13314(13314): 1–7.
- [53] Silvia Truscello, Greet Kerckhofs, Simon Van Bael, Grzegorz Pyka, Jan Schrooten, and Hans Van Oosterwyck. Prediction of permeability of regular scaffolds for skeletal tissue engineering: a combined computational and experimental study. *Acta biomaterialia*, 8(4):1648–1658, 2012.
- [54] Simon Van Bael, Yoke Chin Chai, Silvia Truscello, Maarten Moesen, Greet Kerckhofs, Hans Van Oosterwyck, J-P Kruth, and Jan Schrooten. The effect of pore geometry on the in vitro biological behavior of human periosteum-derived cells seeded on selective laser-melted ti6al4v bone scaffolds. *Acta biomaterialia*, 8(7):2824–2834, 2012.
- [55] Claudia Wittkowske, Gwendolen C Reilly, Damien Lacroix, and Cecile M Perrault. In vitro bone cell models: impact of fluid shear stress on bone formation. *Frontiers in bioengineering and biotechnology*, 4:87, 2016.
- [56] Nan Yang, Yanling Tian, and Dawei Zhang. Novel real function based method to construct heterogeneous porous scaffolds and additive manufacturing for use in medical engineering. *Medical engineering & physics*, 37(11):1037–1046, 2015.
- [57] Dong J Yoo. Porous scaffold design using the distance field and triply periodic minimal surface models. *Biomaterials*, 32(31):7741–7754, 2011.
- [58] Amir A Zadpoor. Bone tissue regeneration: the role of scaffold geometry. *Biomaterials science*, 3(2):231–245, 2015.